DRAFT VERSION AUGUST 1, 2016
Preprint typeset using LaTeX style emulateapj v. 5/2/11

arXiv:1605.09261v2 [astro-ph.CO] 29 Jul 2016

AMIBA: CLUSTER SUNYAEV-ZEL'DOVICH EFFECT OBSERVATIONS WITH THE EXPANDED 13-ELEMENT ARRAY

KAI-YANG LIN[1], HIROAKI NISHIOKA[1], FU-CHENG WANG[2], CHIH-WEI LOCUTUS HUANG[1], YU-WEI LIAO[1], JIUN-HUEI PROTY WU[2], PATRICK M. KOCH[1], KEIICHI UMETSU[1], MING-TANG CHEN[1], SHUN-HSIANG CHAN[2], SHU-HAO CHANG[1], WEN-HSUAN LUCKY CHANG[2], TAI-AN CHENG[2], HOANG NGOC DUY[1], SZU-YUAN FU[2], CHIH-CHIANG HAN[1], SOLOMON HO[3], MING-FENG HO[2], PAUL T.P. HO[1,4], YAU-DE HUANG[1], HOMIN JIANG[1], DEREK Y. KUBO[3], CHAO-TE LI[1], YU-CHIUNG LIN[2], GUO-CHIN LIU[5], PIERRE MARTIN-COCHER[1], SANDOR M. MOLNAR[1], EMMANUEL NUNEZ[3], PETER OSHIRO[3], SHANG-PING PAI[2], PHILIPPE RAFFIN[3], ANTHONY RIDENOUR[3], CHIA-YOU SHIH[3], SARA STOEBNER[3], GIAP-SIONG TEO[2], JIA-LONG JOHNNY YEH[2], JOSHUA WILLIAMS[3], AND MARK BIRKINSHAW[6]

Draft version August 1, 2016

ABSTRACT

The Yuan-Tseh Lee Array for Microwave Background Anisotropy (AMiBA) is a co-planar interferometer array operating at a wavelength of 3 mm to measure the Sunyaev-Zel'dovich effect (SZE) of galaxy clusters at arcminute scales. The first phase of operation – with a compact 7-element array with 0.6 m antennas (AMiBA-7) – observed six clusters at angular scales from $5'$ to $23'$. Here, we describe the expansion of AMiBA to a 13-element array with 1.2 m antennas (AMiBA-13), its subsequent commissioning, and cluster SZE observing program. The most noticeable changes compared to AMiBA-7 are (1) array re-configuration with baselines ranging from 1.4 m to 4.8 m, allowing us to sample structures between $2'$ and $10'$, (2) thirteen new lightweight carbon-fiber-reinforced plastic (CFRP) 1.2 m reflectors, and (3) additional correlators and six new receivers. Since the reflectors are co-mounted on and distributed over the entire six-meter CFRP platform, a refined hexapod pointing error model and phase error correction scheme have been developed for AMiBA-13. These effects – entirely negligible for the earlier central close-packed AMiBA-7 configuration – can lead to additional geometrical delays during observations. Our correction scheme recovers at least $80\pm5\%$ of point source fluxes. We, therefore, apply an upward correcting factor of 1.25 to our visibilities to correct for phase decoherence, and a $\pm5\%$ systematic uncertainty is added in quadrature with our statistical errors. We demonstrate the absence of further systematics with a noise level consistent with zero in stacked uv-visibilities. From the AMiBA-13 SZE observing program, we present here maps of a subset of twelve clusters with signal-to-noise ratios above five. We demonstrate combining AMiBA-7 with AMiBA-13 observations on Abell 1689, by jointly fitting their data to a generalized Navarro–Frenk–White (gNFW) model. Our cylindrically-integrated Compton-y values for five radii are consistent with results from the Berkeley-Illinois-Maryland Array (BIMA), Owens Valley Radio Observatory (OVRO), Sunyaev-Zel'dovich Array (SZA), and the *Planck* Observatory. We also report the first targeted SZE detection towards the optically selected cluster RCS J1447+0828, and we demonstrate the ability of AMiBA SZE data to serve as a proxy for the total cluster mass. Finally, we show that our AMiBA-SZE derived cluster masses are consistent with recent lensing mass measurements in the literature.

Subject headings: cosmology: cosmic background radiation — galaxies: clusters: general — instrumentation: interferometers

1. INTRODUCTION

The Yuan-Tseh Lee Array for Microwave Background Anisotropy (AMiBA)[7] is a platform-mounted interferometer operating at a wavelength of 3 mm to study arcminute-scale fluctuations in the cosmic microwave background (CMB) radiation (Ho et al. 2009). While the primary anisotropies in the CMB are measured to high accuracy over the whole sky, and the cosmological parameters are tightly constrained by the Wilkinson Microwave Anisotropy Probe (WMAP, Hinshaw et al. 2013) and the *Planck* mission (Planck Collaboration et al. 2015a), the arcminute-scale fluctuations resulting from secondary perturbations along the line of sight are less resolved. One of the most prominent perturbations comes from galaxy clusters, which are the largest bound objects in the framework of cosmological hierarchical structure formation. Hot electrons that reside in the deep gravitational cluster potential scatter off and transfer energy to the cold CMB photons. This Sunyaev-Zel'dovich effect (SZE, Sunyaev & Zeldovich 1970, 1972, see also Birkinshaw 1999; Carlstrom et al. 2002) is directly related to the density and temperature of the hot cluster gas, which traces the underlying dark matter distribution, and is complementary to information derived from X-ray, gravitational lensing, and kinematic observations of the galaxy cluster. The AMiBA observing wavelength of 3 mm was chosen to minimize the combined contamination from both radio sources and dusty galaxies.

The SZE is nearly redshift-independent and is, thus, suitable to search for high-redshift galaxy clusters. To date, several extensive blind SZE surveys with catalogs of hundreds of clusters have been conducted by the Atacama Cosmology Telescope (ACT, Hasselfield et al. 2013), the South Pole Telescope (SPT, Bleem et al. 2015), and the *Planck*

[1] Academia Sinica Institute of Astronomy and Astrophysics, P.O. Box 23-141, Taipei, Taiwan 106; kylin@asiaa.sinica.edu.tw
[2] Physics Department, National Taiwan University, Taipei, Taiwan 106; jhpw@phys.ntu.edu.tw
[3] ASIAA Hilo Office, 645 N. A'ohoku Place, University Park, Hilo, Hawaii 96720, U.S.A.
[4] East Asian Observatory, 660 N. Aohoku Place, University Park, Hilo, Hawaii 96720, U.S.A.
[5] Department of Physics, Tamkang University, 251-37 Tamsui, New Taipei City, Taiwan
[6] HH Wills Physics Laboratory, University of Bristol, Tyndall Avenue, Bristol BS8 1TL, UK
[7] http://amiba.asiaa.sinica.edu.tw

mission (Planck Collaboration et al. 2015b). These surveys generally have arcminute scale resolutions and are, in some cases, able to resolve the pressure profile of the hot cluster gas. Compared to X-ray-selected cluster samples, SZE-selected samples tend to have shallower cores, hinting at a population at dynamically younger states that may have been under-represented in X-ray surveys (Planck Collaboration et al. 2011a).

The AMiBA is sited within the Mauna Loa Observatory at an altitude of $3,400$ m on the Big Island of Hawaii. The telescope consists of a novel hexapod mount (Koch et al. 2009) with a carbon-fiber-reinforced polymer (CFRP) platform (Raffin et al. 2004, 2006; Koch et al. 2008; Huang et al. 2011). Dual linear polarization heterodyne receivers (Chen et al. 2009), powered by high electron-mobility transistor (HEMT) low-noise amplifiers (LNAs) and monolithic microwave integrated circuit (MMIC) mixers, are co-mounted on the steerable platform. A wideband analog correlator system (Li et al. 2010) correlates, integrates, and records the signal on the platform.

The interferometer was built and operated in two phases. The first phase was comprised of seven close-packed 0.6 m antennas (hereafter AMiBA-7, Ho et al. 2009). Scientific observations were conducted during 2007 - 2008, and six galaxy clusters in the redshift range of 0.09 to 0.32 were mapped with an angular resolution of $6'$(Wu et al. 2009). We carefully examined noise properties (Nishioka et al. 2009), system performance (Lin et al. 2009), and contamination by CMB and foreground sources (Liu et al. 2010) in our science data. Huang et al. (2010) derived the cylindrically-integrated Compton-y parameter Y_{2500} of the small sample and found consistent scaling relations with X-ray-derived temperature T_e, mass M and luminosity L_x (all within r_{2500}). Liao et al. (2010) further tested recovering temperature T_e, gas mass M_{gas}, and total mass M_{tot} of the cluster from AMiBA-7 data using different cluster gas models and found the results to be also consistent with values in the literature. Four of the six clusters also had Subaru weak-lensing observations, and Umetsu et al. (2009) derived gas fraction profiles from the SZE and lensing mass data.

The second phase expanded the array to thirteen 1.2 m antennas (hereafter AMiBA-13) with a synthesized beam of $2.'5$, enhancing the ability to detect clusters at higher redshifts. Molnar et al. (2010b) tested the ability of AMiBA-13 to constrain the temperature distribution for non-isothermal β-model mock observations of hydrodynamic simulations and concluded that the scale radius of the temperature distribution can be constrained to about 50% accuracy. Scientific observations using AMiBA-13 started in mid-2011 and ended in late 2014. The targets observed with AMiBA-13 include (a) the six clusters observed with AMiBA-7, (b) high-mass clusters selected from the Cluster Lensing And Supernova survey with Hubble (CLASH, Postman et al. 2012) sample, and (c) a small sample drawn from the Red-sequence Cluster Survey 2 (RCS2, Gilbank et al. 2011).

We will describe changes made to the instrument in Section 2 and demonstrate the performance and systematics of the array in Section 3. In Section 4, we will detail our observing strategy, calibration, and data flagging. Section 5 discusses radio source contamination and interpretation of our cluster SZE data. Our conclusions are summarized in Section 6. We adopt a flat Λ cold dark matter (ΛCDM) cosmology with $H_0 = 67.1\,\mathrm{km\,s^{-1}\,Mpc^{-1}}$, $\Omega_\mathrm{m} = 0.3175$, and $T_\mathrm{CMB} = 2.725$ K (Planck Collaboration et al. 2014).

Table 1
Comparison of AMiBA-7 and AMiBA-13

	AMiBA-7	AMiBA-13
Number of Antennas	7	13
Number of Baselines	21	78
Polarizations	XX & YY	XX & YY
Antenna Diameter (m)	0.6	1.2
Baseline Range (m)	$0.6-1.2$	$1.4-4.8$
Primary Beam (FWHM)	$22'$	$11'$
Synthesized Beam (FWHM)	$6'$	$2.'5$
Elevation Limit (deg)	30	40[a]
Point Source Sensitivity (mJy/$\sqrt{\mathrm{hr}}$)	64	8
Extended Source Sensitivity (μK/$\sqrt{\mathrm{hr}}$)	238	174

[a] The CFRP platform was repaired prior to the AMiBA-13 observations. After the repair, we limited the operating range of the hexapod as a safeguard.

2. CHANGES COMPARED TO AMIBA-7

To complete the 13-element array, six additional receivers were built with design and component specifications identical to the first seven receivers. All of the new receivers, except one, have noise temperatures around $55-75$ K which is comparable to the old receivers (Chen et al. 2009), while the one exception shows a higher noise temperature at 85 K. Additional correlators and intermediate frequency (IF) distribution networks were also built following the 7-element design (Li et al. 2010). The new correlators are housed in the same enclosures on the platform that were previously only partially populated by the 7-element correlators. Table 1 summarizes the changes between AMiBA-7 and AMiBA-13. The system performance is discussed in Section 3.

2.1. *Array Configuration*

Figure 1 shows the AMiBA-7 and AMiBA-13. Equipped now with larger antennas, six of the original receivers were relocated further out on the platform. Similar to the 7-element array, the 13-element array has a hexagonally close-packed configuration. Two choices of shortest baseline lengths are available for the 1.2 m diameter reflectors, namely 1.2 m and 1.4 m. We chose the configuration with the 1.4 m separations, which has about a 10 times lower cross-talk between neighboring dishes (a measured -135 dB on the 1.4 m versus an estimated -125 dB on the 1.2 m baseline; Koch et al. 2011). Figure 2 shows the array configuration in the platform coordinate system and the corresponding instantaneous uv-coverage assuming a single frequency of 94 GHz.

Compared to the close-packed configuration, the 1.4 m separation between dishes also helps to suppress the primary CMB leakage, in favor of cleaner cluster SZE observations. Given the angular power spectrum C_l of the CMB, we can estimate the rms fluctuation that is picked up by a baseline following the steps outlined in Liu et al. (2010) as

$$\langle V^2(u_b,v_b)\rangle = \int dudv\tilde{A}^2(u_b-u,v_b-v)C_l \times\left(1-\cos[2\pi(u\Delta x+v\Delta y)]\right), \quad (1)$$

where (u_b,v_b) corresponds to the center of a particular baseline. The modulating factor $(1-\cos[2\pi(u\Delta x+v\Delta y)])$ comes from subtracting the trailing patch from the target patch, with a sky separation of $(\Delta x,\Delta y)$. The 'two-patch' observation scheme is discussed in more detail in Section 4.2. The CMB leakage is stronger for shorter baselines. With the 1.2 m

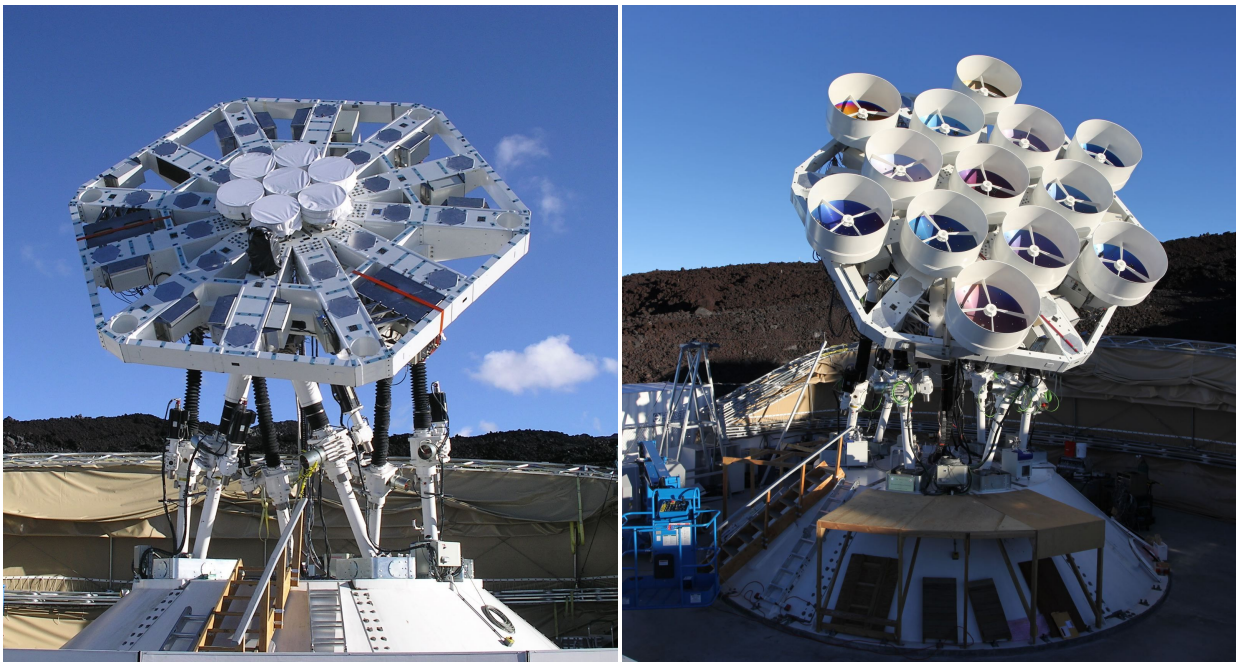

Figure 1. Pictures of the AMiBA-7 (left) and AMiBA-13 (right). The AMiBA-7 had 0.6 m antennas in a closely-packed configuration with shortest spacing 0.6 m. The AMiBA-13 has 1.2 m antennas with a shortest spacing of 1.4 m. Visible in the background is the retractable shelter that is closed when the telescope is not in operation.

dishes, we estimate that the 1.2 m baseline has an rms fluctuation of ~ 20 mJy from the CMB. The 1.4 m baseline has about a factor of two lower level of rms fluctuation, at ~ 11 mJy. By comparison, the AMiBA-7 configuration (0.6 m dishes separated by 0.6 m) had fluctuations of roughly 170 mJy at the 0.6 m and 24 mJy at the longer 1.2 m baseline. Figure 3 shows the unmodulated CMB power spectrum and a two-patch modulated spectrum with a typical patch separation of $\Delta x = 45'$ and $\Delta y = 0$. Also shown are the footprints in uv-space, accumulated in each annular bin, as a function of multipole-l for both AMiBA-13 and AMiBA-7 to show where the sensitivity lies.

2.2. 1.2 *m Reflector*

The design of AMiBA has the 1.2 m diameter f/0.35 Cassegrain reflector (Table 2, Koch et al. 2011) mounted onto the top plate of the receiver assembly while the receiver itself is directly attached onto the CFRP platform. This avoids having the reflector directly on the platform and eliminates any additional misalignment between reflector optical axis and the receiver feed. A detailed Finite-Element Analysis (FEA) of the entire CFRP reflector helped to reduce the weight to a final 25 kg from an original prototype that weighed almost 50 kg. An equally stiff antenna made out of aluminium would be at least 35 kg. CFRP was chosen as a lightweight material in order to minimize torque and structural deformations under various load cases. Excellent structural behavior is found from the FEA for the lightweight CFRP reflector. Thermal load cases introduce tilts in the optical axis of only around $1''$. Strong winds of 10 m/s lead to tilts between $0.5'$ and $\sim 1'$ depending on pointing elevation. Deformation under gravity is largest, at about 1 arcmin, at the lowest operating elevation of 30°. All these tilts are within 10% of the 11-arcmin full width at half maximum (FWHM) of the antennas, and introduce less than 3% of loss.

Primary and secondary mirror surfaces were measured after manufacturing. Fitting for a primary paraboloid and a secondary hyperboloid shows random surface rms errors of about 30 μm and 15 μm, respectively. Following Ruze (1966), these small manufacturing errors keep the surface efficiencies at 98.5% and 99% for primary and secondary at a frequency of 94 GHz. After assembly, the resulting alignment errors are between 50 μm and 100 μm which reduce the aperture efficiency by less than 1%. The final antenna aperture efficiency, composed of a series of independent factors — feed-horn illumination efficiency, secondary mirror and support leg blockage efficiency, surface roughness efficiency, feed spillover efficiency, focus error efficiency, cross-polarization efficiency, diffraction and ohmic losses — is estimated to be about 0.6, dominated by the feed spillover efficiency of < 0.78 (Koch et al. 2011). Both primary and secondary mirrors are aluminum-coated in vacuum with a homogeneous aluminum layer of about 2 μm. Immediately after the aluminum sputtering an 0.3-μm TiO_2 layer is added for protection against oxidation, abrasion, peeling off and accidental pointing towards the Sun.

The antenna beam pattern was measured in the far field by scanning a fixed thermally stabilized 90 GHz source. The antenna response was previously simulated including the complete feed horn-antenna system with a corrugated feed horn with a semiflare illumination angle of 14° with a parabolic illumination grading with a -10.5 dB edge taper. Our measurement confirms the simulated main lobe with an $11'$ FWHM. The location of the first side lobe is confirmed at $18'$, while its level is about 2–4 dB higher than expected, peaking around -16 to -18 dB (Koch et al. 2011).

Finally, close-packed antenna configurations can cause cross-talk problems in weak cluster SZE and CMB signals. Our estimated tolerable level of cross-talk is around -127 dB (Koch et al. 2011; Padin et al. 2000). In order to minimize this signal, a cylindrical shielding baffle is added to the reflector, similar to the earlier 0.6 m antennas. Effectively re-

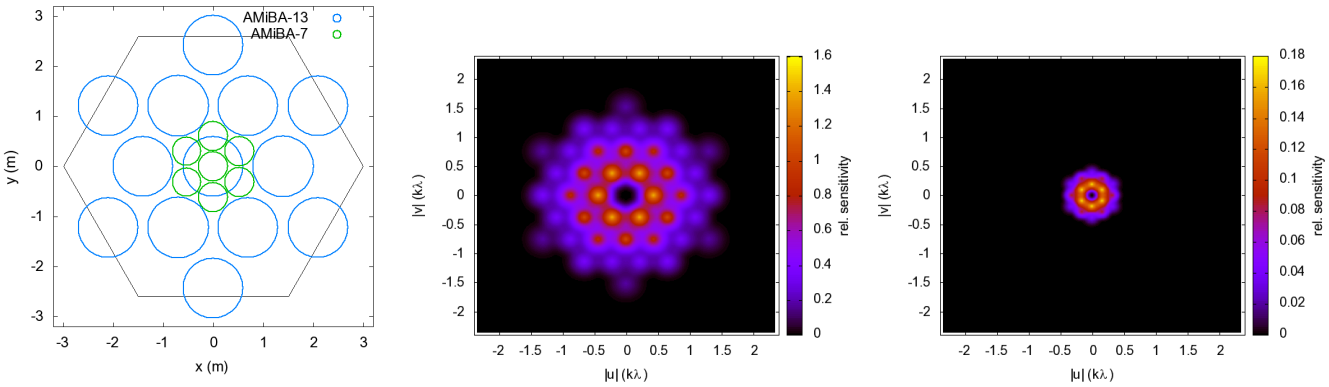

Figure 2. Left panel: array configuration in platform coordinates. The larger circles represent the dish sizes and locations of the 13-element array. For comparison, the smaller circles in the center of the platform indicate where the AMiBA-7 antennas were. Large hexagon identifies the edge of the platform. Middle and right panel: instantaneous uv-coverage of AMiBA-13 and AMiBA-7, respectively, with their relative sensitivities in color scales.

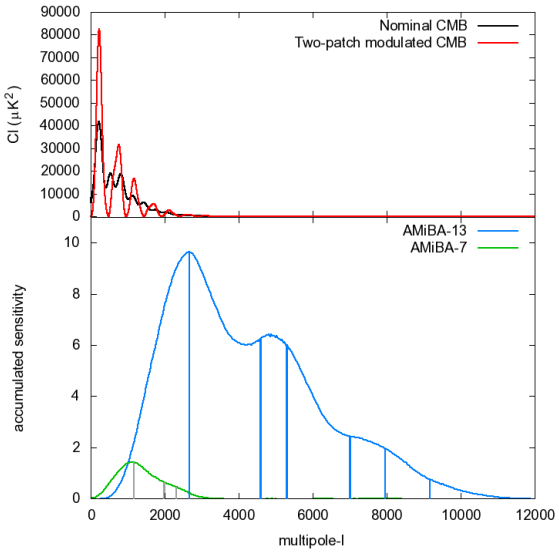

Figure 3. Top panel: CMB primary anisotropy spectrum (black) and modulated spectrum after a two-patch subtraction with a separation of 45′(red). Bottom panel: accumulated sensitivity in uv-space, summed in each annulus of multipole-l, for AMiBA-13 and AMiBA-7, respectively. The vertical lines denote the centers of the baselines. The conversion from baseline length to multipole-l assumes a single frequency of 94 GHz.

duced cross-talk signals were, indeed, verified on the operating AMiBA platform where one antenna was used as an emitter with a $\sim$ 10 dBm source while in neighbouring antennas with different baseline lengths the weak cross-talk signal was measured with a spectrum analyzer. On the shortest 1.4 m baseline, cross-talk signals of ~ -135 dB and ~ -115 dB were measured with and without the shielding baffle, respectively. A further reduced signal of ~ -145 dB was found when the separation was increased to 2.8 m (Koch et al. 2011). For baselines longer than 2.8 m, the cross-talk is below our detection limit of -145 dB. Besides shielding the reflectors, an additional measure to further reduce unwanted scattered signals was taken by optimizing the shape of the secondary mirror support leg structure. A triangular roof is added on the lower side of the feed leg to terminate scattered light on the sky (Lamb 1998, ALMA Memo 195; Cheng et al. 1998, ALMA Memo 197)[8]. As a result, cross-like features in the measured beam patterns at the locations of the feed leg are

[8] Main ALMA Memo Series: http://library.nrao.edu/alma.shtml

Table 2
Characteristics of 1.2 m Reflector

Parameters	Values
Reflector Type	Cassegrain
Primary Diameter	1.2 m
FWHM of Beam Pattern	11′
Primary Focal Ratio	0.35
Secondary Diameter	0.19 m
Effective Focal Ratio	2.04
Final Focal Position	At vertex of primary
Illumination Edge Taper	−10.5 dB
Antenna Efficiency	60 %
Height of Baffle above Secondary Edge	0.36 m

reduced to an amplitude of about 1 dB compared to more apparent peaks around 3 dB in the earlier 0.6 m antennas. Additional details of the 1.2 m Cassegrain antenna can be found in Koch et al. (2011).

3. COMMISSIONING

3.1. *Delay Correction*

After new receiver units and IF distributions are installed, the path lengths need to be adjusted so that signals from within the field of view can be adequately sampled by our lag-correlator. The path length difference, excluding the geometric delays, is referred to as the instrumental delay throughout this work. The lag-correlator has four mixers, each separated by 25 ps delay, corresponding to the Nyquist sampling rate for a bandwidth of 20 GHz (Li et al. 2010). The accessible delay range is, thus, around $\pm$50 ps. In the case of AMiBA-13, to allow a 5 m baseline to observe the entire 11′field-of-view, the instrumental delay should be controlled within $\pm$22 ps. Following the method outlined in Lin et al. (2009), instrumental delays were measured on the platform, from feed horn to correlator, using two methods that will be described below. Cables were then inserted into the IF path in order to compensate for the delays.

In the first method, we set up a broadband noise source simultaneously emitting toward two receivers (without the 1.2 m dishes) at a time. We then moved the noise source along the baseline and recorded the fringe as a function of the geometric delay. The difference between the center of the baseline and the position where the fringe peaked, marked the instrumental delay between the pair of receivers. Additionally, by Fourier transforming the fringe with respect to the geometric delay, we could also obtain a measure of the band-

pass response function, modulated by the spectral shape of the noise source. The bandpass of the new baselines was, indeed, similar to the ones previously measured for AMiBA-7, with a comparable effective bandwidth around $7-13$ GHz.

The above mentioned method is powerful but time consuming. It was performed once on all functioning baselines to establish a reference bandpass functions. During subsequent iterations of delay-tuning, we relied on the second method, in which we scanned the array, without the dishes, across the Sun and recorded the fringes. Without the dishes, the FWHM of the feed horn is about 20° (Koch et al. 2011). The resultant fringe is a convolution of the point-source fringe with the brightness distribution of the Sun, which we assumed to be a circular top-hat function. Depending on the instrumental delay τ^{inst}, the measured fringe peak can appear before or after the expected one with an angular offset θ described by

$$\theta B\cos\alpha = c\tau^{\rm inst}\,, \tag{2}$$

where $B\cos\alpha$ is the projected baseline length along the scanning direction. c is the speed of light. However, for baselines that are almost perpendicular to the scan, the fringes would be too slow, θ too big, and $\tau^{\rm inst}$ thus poorly determined. Therefore, for each measurement we scanned the Sun in four directions, namely along the right ascension (R.A.), along the declination (decl.), and two directions in between, so that all baselines had a sufficiently high fringe rate in a few of the scans. In this way, we could probe a large delay range for each baseline.

For each polarization (XX or YY), two coaxial cables from the same IF channel are fed to the correlator rack, with one feeding a "row" of correlators from the "front" and the other feeding a "column" from the "back". We simplify the measured delays as the difference of electrical lengths from the IF channels L_k, or

$$\tau_i^{\rm inst} = \left[\delta_{f(i)k} - \delta_{b(i)k}\right] L_k \equiv D_{ik}L_k\,, \tag{3}$$

where $\delta_{f(i)k}$ and $\delta_{b(i)k}$ are Kronecker deltas that select the IF paths corresponding to the "front" $f(i)$ and "back" $b(i)$ of the i-th correlator. For AMiBA-13, there are 78 delays measured for each polarization ($i\in[1,78]$). Since the cables connecting to the "front" are independent from the ones connected to the "back" of the correlator rack, their electrical lengths are solved independently. There are, thus, 24 electrical lengths to solve ($k\in[1,24]$), in which 12 "fronts" connect to antenna 1 through 12 and 12 "backs" connect to antenna 2 through 13, respectively. We also note that there are power dividers and cables inside the correlator rack in order to further distribute the signals to the 78 correlators. The electrical lengths of these paths, while short, may not be equal. These delays are included in the measured $\tau_i^{\rm inst}$ but they are not explicitly represented in Equation (3) because they cannot be adjusted. This is likely the major source of our residual delays.

We used the LAPACK routine SGESVD to perform a singular value decomposition (SVD) of the sparse matrix D_{ik}, zeroing singular values smaller than 10^{-6}. We then constructed the pseudo-inverse matrix $D_{\rm SVD}^{-1}$ to find the estimated electrical lengths $\tilde{L}_k$ through

$$\tilde{L}_k = \left(D_{\rm SVD}^{-1}\right)_{ki}\tau_i^{\rm inst}\,. \tag{4}$$

Adjustments to the electrical lengths were done by installing short cables of corresponding lengths to each of the IF paths. The measurement and adjustment process was iterated several times until the residuals could not be further improved. Because of measurement uncertainties, imperfection of the pseudo-inverse matrix reconstruction, and the additional delays mentioned above, exact solutions are not possible. Consequently, some of the correlators ended up having much larger residual delays than the others. The rms scatter of these residual delays is 22 ps, while the maximum of these residuals can be up to twice this amount. However, we note that even correlators with the largest residual delays are still capable of detecting a source that is not too far off the pointing center of the platform, which is also the phase center after calibration. Correlators that have large delays can be very inefficient when additional geometrical delays are present. In this case, they will be flagged. They amount to about 10 % of the total number of correlators. Contributions to the geometrical delays come from target offsets from the phase center (offset observations, extended objects, or platform pointing errors) and the platform deformation. Both effects are discussed in the following sections. The overall effect on phase error is discussed in Section 3.5.

3.2. *Platform Deformation*

AMiBA uses a CFRP platform as a lightweight solution to host the entire array and the correlator system on top of the hexapod mount (Raffin et al. 2004). Ideally, the universal joints (u-joints) of the hexapod should be held rigidly in two planes (one for the upper u-joints, and one for the lower u-joints). While the lower u-joints are fixed to the supporting cone, a steel interface ring beneath the platform is used to hold the upper u-joints. However, the interface ring was found to be not rigid enough to entirely absorb the differential forces from the six heavy legs, in addition to the gravitational forces from the platform and equipment at tilted orientations. As a result, the platform deforms as a function of its orientation, including the pointing in azimuth (az) and elevation (el), and a rotation along the pointing axis (hereafter referred to as $hexpol$). The deformation was measured in several photogrammetry campaigns, sampling the (az,el,$hexpol$)-parameter space with hundreds of photos of the platform (with several hundred reflective targets). The results show that the deformation is, indeed, repeatable within the measurement uncertainty of $\sim 50\,\mu$m in rms. Figure 4 shows an example of the deformation pattern at two different elevations. Generally, the deformation along the pointing direction appears to be saddle-like, with a functional form $\sim A\cdot(x^2-y^2)$, where A is an amplitude and x and y are coordinates in a platform reference frame. Across the sample of photogrammetry-measured positions, the deformation shows characteristic properties: deformations grow with radius, reaching maximum values at the edge of the platform. Moreover, the deformation amplitude increases with lower elevation and larger platform $hexpol$ rotations. The saddle pattern rotates with a roughly constant amplitude as the hexapod changes its azimuth pointing (Liao et al. 2013; Huang et al. 2008; Koch et al. 2008). Relative to the neutral orientation (pointing toward zenith), the maximum normal deformation at the edge of the platform increases with decreasing elevation and can reach a value as high as 1.5 mm (Huang et al. 2008; Koch et al. 2008), or half of our observing wavelength.

In order to define a tolerance for deformation, for simplicity, we model the deformation-induced phase error with a Gaussian random distribution and an rms error of σ. The coherence efficiency is, thus, $\eta_c = \exp(-\sigma^2/2)$. When $\sigma = 2\pi/20$ – which corresponds to an rms deformation of a wavelength $\lambda/20$ ($\lambda = 3$ mm) or roughly 150 μm at our fre-

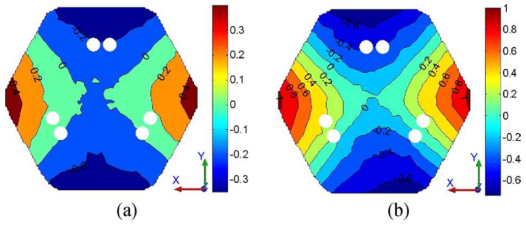

Figure 4. Photogrammetry-measured platform deformation with respect to zenith position at different elevations (a) $el = 60°$ and (b) $el = 30°$, both with $az = 0°$ and $hexpol = 0°$. Color scale is in units of mm. The three pairs of white filled circles indicate the locations of the u-joints on the underside of the platform.

quency – the efficiency is about 95%. We have set this as our nominal tolerance level for residual deformation errors.

Huang et al. (2011) further investigated the platform deformation using FEA. They confirmed the insufficient stiffness to be the dominant cause of our deformation problem. However, further investigation also determined that given our constraints on load capacity of the hexapod mount and the existing shelter size and dimensions (Figure 1), neither a space frame platform built with steel nor a space frame built with CFRP can provide the required stiffness to keep the deformations within the 150 μm rms error tolerance across all observing orientations. Therefore, we kept the platform and decided to remedy the problem through modelling and post-processing of the collected data.

The major effect of the platform deformation on a co-planar interferometry observation is the addition of a pointing-dependent geometric delay. Since AMiBA uses an analog delay-correlator (with four lags) to generate two spectral channels that cover $86 - 102$ GHz in the radio frequency (RF), the geometric delay induces a phase change at the center of each frequency band and a band-smearing effect in each 8 GHz channel. The phase change can be calculated and removed if we know how the platform deforms as a function of pointing. In order to model the band-smearing effect, on the other hand, precise knowledge of the source spectrum and the bandpass response is required for each baseline. However, Lin et al. (2009) showed that even though the bandpass could be characterised to a spectral resolution of ~ 0.1 GHz, it failed to model the band-smearing effect. Therefore, in the current work, the band-smearing effect remains a systematic factor that reduces the peak flux of a point source by up to 10 % at the lowest elevation of $el = 40°$.

Liao et al. (2013) summarize in detail the method that we use to measure and model the platform deformation. Moreover, they demonstrate its effectiveness when applied to planets and a few radio point sources. In short, we find changes in the large-scale deformation pattern – measured by photogrammetry across the entire platform – to correspond well to changes in the local tangent of the surface. Therefore, it is possible to use and correlate two optical telescopes (OTs; mounted on two different locations on the platform) and perform an all-sky pointing error analysis to find out the relative change between the local tangents of the two OTs. This information is then used to solve for an all-sky deformation model. Following the trajectory of Jupiter, it was verified that geometrical delays predicted by this model match the measurements to within ± 0.2 mm. Considering the decoherence effect due to the phase error, it was further shown that when applying this deformation correction, we are able to recover at least 95 % of the remaining flux, after considering the band-smearing loss mentioned above, compared to a mere 75 % recovery without the deformation correction.

It is important to note that, although the platform deformation has been the same since the beginning of the AMiBA project, the earlier AMiBA-7 observations utilized only a small central part of the platform (Figure 1) where the deformation-induced geometrical delay is within 150 μm in rms and the induced loss is less than 5%. The earlier AMiBA-7 science results are, thus, unaffected by the platform deformation problem.

3.3. *Antenna Alignment*

Another effect of the platform deformation that impacts a co-planar array is the changing alignment between antennas. These alignments were measured by scanning a planet (Jupiter or Saturn) along the R.A. and decl. directions and recording their fringes. On top of the intrinsic fringe envelope described in Section 3.1, the fringe envelope for each baseline is modulated by the combined beam attenuation of the two antennas that form its baseline. Note that longer baselines have faster fringes and narrower intrinsic envelopes compared to the primary beam. Therefore, any residual instrumental delay may shift the position of the intrinsic envelope and bias the measurement of the beam center. Such baselines are then flagged and not used to solve for the misalignments. On the other hand, baselines with shorter *projected* lengths along the scanning direction have slower variations in the intrinsic fringe envelopes, and the primary beam attenuation dominates the fringe envelope. We then fit a Gaussian to the fringe envelope to determine the offset of the combined beam center along the scanning direction. In some cases, baselines with too slow a fringe rate, showing no more than two fringes within the primary beam, are also discarded because their envelopes are distorted by under-sampling in delay by the lag-correlator. Lastly, since the combined primary beam attenuation should affect both polarization in the same way, we look for and flag any inconsistency between the XX and YY beam center measurements that may indicate an excessive instrumental delay for one polarization or other faults in the fringe records.

The combined beam center of one baseline can be approximated by $\mathbf{C} = (\mathbf{P}_a + \mathbf{P}_b)/2$ as in the case of Gaussian beams, where $\mathbf{P}_a$ and $\mathbf{P}_b$ denote beam centers of antenna a and b, respectively. Our two orthogonal scans project the beam centers onto two sets of measurements that can be solved independently. Let x denote the component projected along either R.A. or decl., we then have

$$C_{xi} = \frac{1}{2}\left[\delta_{a(i)k} + \delta_{b(i)k}\right] P_{xk} \equiv M_{ik} P_{xk}\,, \qquad (5)$$

where the subscript i runs through the subset of unmasked measurements out of the 78 baselines, and the subscript k denotes the 13 independent antennas. Similar to what was done in Section 3.1 for delay measurements, we invert the sparse matrix M by the SVD technique and a solution can be found for each scan. Uncertainties in determining the fringe envelope and its centroid position are propagated through the SVD-based matrix inversion to the alignment solutions. We estimate these uncertainties to be about $0\farcm5$ in rms.

Since the platform deformation changes with pointing (see Section 3.2), most importantly with azimuth, the antennas sway as the deformation pattern rotates. Figure 5 shows the alignment solutions of repeated scans while we followed Saturn across the sky in one night. For this plot, only the relative

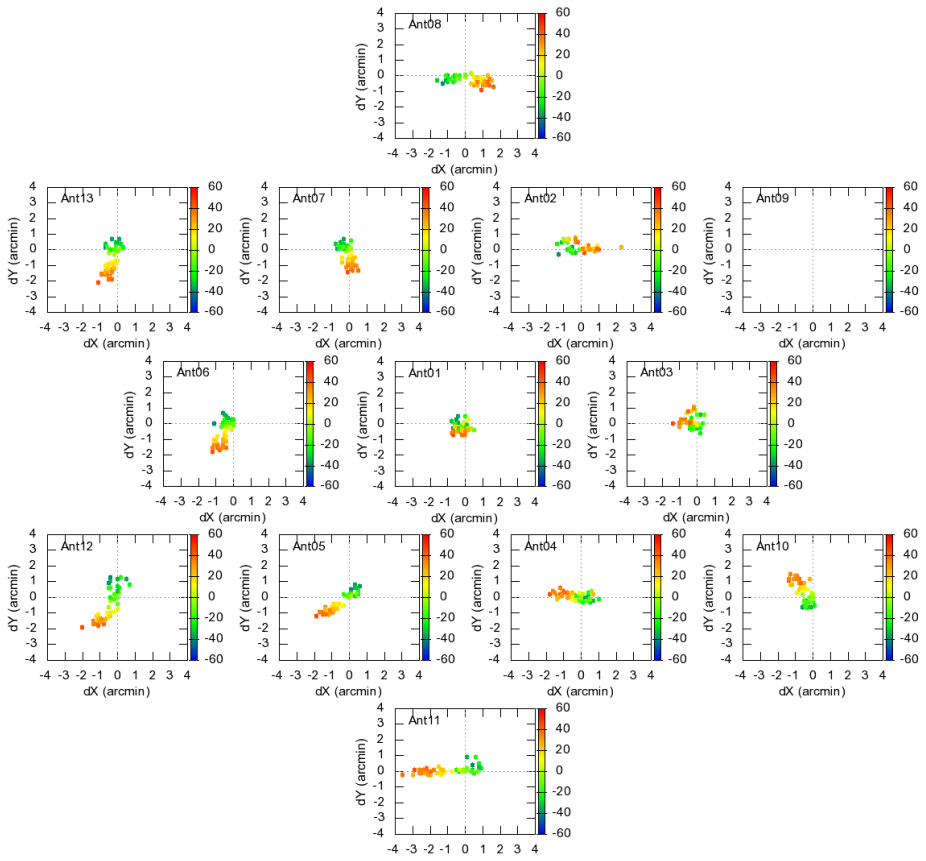

Figure 5. Misalignment of each antenna following the trajectory of Saturn as a function of hour angle of pointing (color scale, units in degree). The declination of Saturn during the observation was roughly $-4°$. The misalignment is plotted in arcminutes projected on the platform. Antenna 09 was off-line during this test. It is shown that, except Antenna 11, all other antennas have their misalignment within $\pm 2'$.

change is shown, referenced to the alignment at transit of Saturn. The result shows that antennas mostly swing within $\pm 2'$, with the extremes at lower elevations. These measured misalignments agree with the photogrammetry-measured deformation amplitudes along the z-direction (Figure 4), i.e., measured maximum amplitudes of about 1.5 mm at the outer platform lead to a tilt of about $1\farcm7$ over a 3 m platform radius. This indicates that the photogrammetry is, indeed, capturing all relevant deformation features.

Antenna misalignments additionally lead to an efficiency loss. Figure 6 shows an example of this loss at lower elevation where the loss is more severe. For a source at the pointing center, the loss is about 7%. It is less if the source is observed at higher elevation.

3.4. *All-Sky Radio Pointing*

Koch et al. (2009) describe how the pointing model of the AMiBA hexapod mount was established with an optical telescope. Further taking into account the parametric model of the platform deformation developed by Liao et al. (2013), we carefully rebuilt the pointing model by removing the tilt of the optical telescope due to the platform deformation in order to achieve a better pointing accuracy as required for the more extended AMiBA-13 array. We further observed a dozen radio sources, selected from the Australia Telescope Compact Array (ATCA) calibrator database[9], that have a listed 3 mm flux density higher than 2 Jy and that are evenly distributed in our observable decl. range in order to evaluate the residual pointing error in *radio* observations. The first round of radio pointing observations revealed a residual error pattern ranging from $0'$to $2'$that slowly varied with pointing. We then fitted a

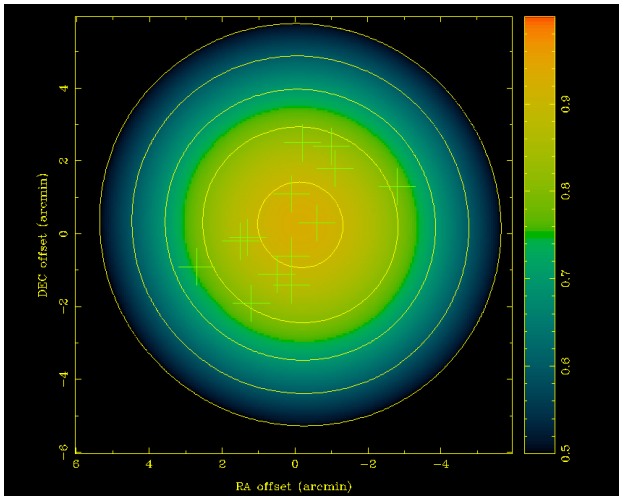

Figure 6. Instance of combined alignment efficiency plot. Green crosses indicate misalignments of the 13 individual antennas in arcminutes. The color scale shows the averaged primary beam attenuation for a source at indicated (R.A., decl.)-offset from the pointing center. Contours denote 0.5, 0.6, 0.7, 0.8, and 0.9 times the ideal-case attenuation, assuming all antennas to be perfectly aligned. For sources without any pointing error (at the center of the plot), the sensitivity is 93%, while the 90% sensitivity region has a radius of about $1'$.

[9] http://www.narrabri.atnf.csiro.au/calibrators/

low-order polynomial function to the pattern and removed it from the pointing model. Figure 7 shows the residual error distribution of the second round of radio pointing observations. It shows that some decl. ranges still have larger pointing errors ($\sim 1'$), but overall the radio pointing error is about $0\farcs4$ in rms. Equally importantly, the pointing repeatability — derived from night-to-night trackings over several hours of the same stars with the OTs — is around $10''$and it sets the limit of achievable pointing error for our telescope. If we assume the pointing error to be truly random with an rms error of $0\farcs4$, for a $2\farcs5$ synthesized beam, the smearing effect leads to a loss of less than 2%. However, since for any given target the pointing error along its track is not random and is seldom symmetric, there can be systematic pointing errors after integration. To alleviate this problem, a companion pointing source within 5° of the target is observed every ∼30 min to monitor the pointing error along the track.

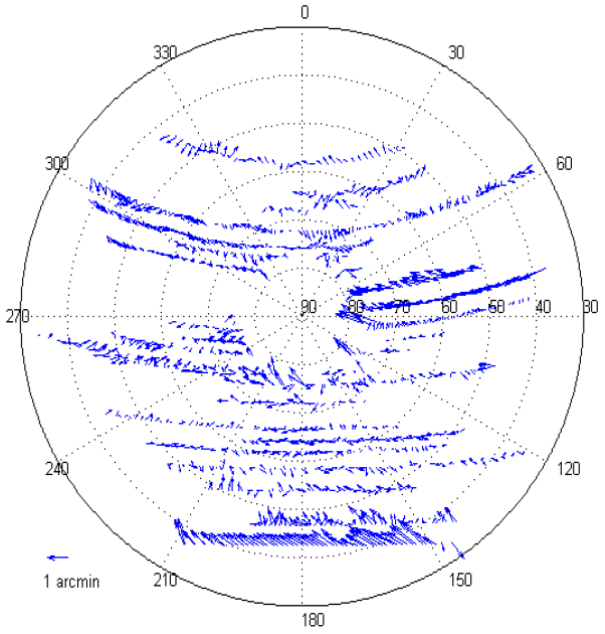

Figure 7. All-sky radio pointing error verification. The chart shows the full azimuth range ($0° \leq az \leq 360°$) and an elevation range down to 30°. Arrows indicate the magnitude and direction of pointing errors. The rms pointing error for observations with $40° < el < 77°$ is $0\farcs4$. Cluster observations are carried out in this elevation range.

3.5. *Phase Error and Flux Correction*

In Section 3.1, we mentioned that correlators that have large residual delays are especially sensitive to additional geometrical delays coming from pointing offset or platform deformation. These correlators are flagged during data processing. However, regardless of the amount of residual delay, all correlators suffer from phase errors and amplitude imbalance between the two spectral channels. The problem arises from wide-band smearing, leakage between the two channels, and leakage between real and imaginary parts in the lag-to-visibility transformation. The error varies with the geometric delays. If there were no pointing error nor platform deformation, the error could be calibrated out with an astronomical source. In practice, amplitude and phase errors occur because of the difference in delay between the calibrator and the target observations. We emphasize that we have modelled and corrected for the "mean" phase shift for each spectral channel corresponding to the platform deformation. The phase error considered here, which originates from the phase slope within each spectral channel, is different. We also note that AMiBA-7, having a much smaller range of deformation errors and shorter baselines, was much less susceptible to the variation of lag-to-visibility errors.

Since large phase and amplitude errors are both symptoms of a large delay, it is possible to select and remove part of the data for better accuracy. An implication of the channel amplitude imbalance is that one of the two spectral channels has a low signal-to-noise ratio and a high noise variance after flux calibration. When the noise variances of two spectral channels are co-added, the resulting variance becomes substantially larger if the imbalance is stronger. By using the inverse of the co-added noise variance as weighting, we can efficiently downweight correlators that have large delays and smearing effects during the calibrator observations. Nevertheless, correlators that were not downweighted still have phase and amplitude errors, especially when observing a target that is further away from the calibrator. We assess the severity of this effect by checking the point source flux-recovery ratio for a few flux standards. Table 3 summarizes the flux errors under various conditions. The typical flux recovery is between 75% and 85% unless the target is close to the track of the calibrator. Therefore, for visibility and flux measurements, we apply a correction factor of 1.25 and also add $\pm 5\%$ of systematic error in quadrature to the thermal noise as the final uncertainty.

4. CLUSTER SZE OBSERVATIONS

4.1. *Cluster Targets*

Cluster targets for our AMiBA-13 observations are drawn from three different samples emphasizing different aspects of cluster studies. The first sample consists of the six clusters observed by AMiBA-7. Here, a combined AMiBA-7 and AMiBA-13 analysis with an improved uv-coverage can place tighter constraints on the cluster gas pressure profiles. The second set of twenty clusters is selected from the CLASH sample, which has exquisite strong-lensing (Zitrin et al. 2015), weak-lensing (Umetsu et al. 2014, 2016; Merten et al. 2015), and X-ray (Donahue et al. 2014) data, as well as 2 mm SZE data (Bolocam, Sayers et al. 2013) with angular scales similar to AMiBA-13, and additional 3 mm SZE data with $\sim 10''$ resolution (MUSTANG, e.g. Mason et al. 2010; Mroczkowski et al. 2012). AMiBA-13 is complementary to these existing SZE data, allowing for joint analyses of the physical processes that govern the hot cluster gas. Finally, before the observing was concluded, seven optically selected cluster candidates were chosen from the Red-sequence Cluster Survey 2 (RCS2, Gilbank et al. 2011) catalog according to their richness indicator B_{gc} and added to our observations. Although the sample is small, we aim at comparing their SZE signals to other X-ray-selected clusters of similar richness and redshift for signs of selection biases. From all these observed targets, twelve clusters show robust detections above 5σ. Coordinates and redshifts of these clusters are listed in Table 4. Their integration times and detection significances are given in Table 5. Figure 8 shows our SZE images of these selected clusters. For each cluster, the uv data were natually weighted and inverted to produce the dirty image. The image was then cleaned with the Miriad[10] task CLEAN, looking for sources

[10] http://www.atnf.csiro.au/computing/software/miriad/

Table 3
Flux-Recovery Ratio

Factors	Recovery Ratio	Remark
Band-smearing (no phase error)	$> 90\%$[a]	
Deformation (without phase correction)	$> 65\%$[a]	Saturn, Jupiter (relative) [b]
Residual deformation (with phase correction)	$> 85\%$[a]	Saturn, Jupiter (relative) [b]
Cross-calibration (with phase correction)	$75 \sim 85\%$	Uranus[c], 3C286[d] (absolute)

[a] Minimum recovery occurs at the elevation limit of 40°.
[b] Using only one "two-patch" near transit to calibrate the entire track of the planet (Saturn or Jupiter).
[c] Flux of Uranus is calculated by assuming a disk brightness temperature of 120 K, from the mean W-band results of WMAP-7 observations (Weiland et al. 2011).
[d] Absolute flux of 3C286 is taken to be 0.91 ± 0.02 Jy (Agudo et al. 2012).

within the FWHM of the primary beam. The primary beam attenuation was not corrected for. In Section 5.1, we will discuss the possibility of point source contamination. However, for the twelve clusters presented here, no significant point source with flux > 1 mJy is expected, and we have made no correction to the data.

4.2. *Observing Strategy*

Cluster observations follow the same "two-patch" procedure outlined for AMiBA-7 observations (Wu et al. 2009), where we track the cluster for three minutes and then move the telescope to a trailing patch that is 3m10s later in R.A. for another three minutes. The on-source and the off-source patches share the same telescope trajectory. Differencing of the two patches efficiently removes the ground pickup and other low-frequency contamination in the system. Since AMiBA-13 has a primary beam of $11'.5$ FWHM, or $\sigma \sim 10'$ if the beam is approximated by a Gaussian, a typical cluster is roughly 3 to 4σ away from the pointing center of the trailing patch, and any cluster pickup is negligible. For targets at higher declinations ($\mathrm{decl.} \gtrsim 60°$), the integration time and the separation between two patches are both doubled to ensure that a possible source leakage to the trailing patch does not bias our measurement of the background level.

A subtle difference with the AMiBA-7 observing procedure is how we choose to populate the uv-plane. The instantaneous uv-coverage of AMiBA is highly redundant due to its six-fold symmetry for most of the baselines. In AMiBA-7, we split a cluster observation into eight parts, each with the platform position angle ($hexpol$) rotated by 7.5° with respect to the sky. Combined with the six-fold symmetry, this procedure densely sampled the azimuthal angle in the uv-plane. However, since typically our cluster signal-to-noise ratio per uv-mode is less than 1 after integration, spreading the integration in the uv-plane does not provide a significant advantage in cluster imaging and modelling. For AMiBA-13, we stopped actively changing the platform position angle and chose to operate the mount in its most balanced orientation in order to minimize the platform deformation. As we track a target, the sky rotates relative to the platform, and so does the uv-coverage. The rotation is within ±15° for most of our cluster observations and has a high concentration within ±5°. The resulting synthesized beam is, thus, less circular as compared to the AMiBA-7 beam. This is especially the case when some antennas are offline during an observation.

4.3. *Calibration*

Similar to AMiBA-7, the flux and gain calibration of AMiBA-13 is done by observing Jupiter and Saturn for at least one hour each night. All calibration observations are also done in the "two-patch" observing mode with four minutes of integration per patch and a 4m10s separation in R.A. A one-hour observation provides seven sets of two-patch data that are used to gauge the performance of each baseline, including phase scatter over time and phase consistency between the two spectral channels.

To calculate the flux density of Jupiter and Saturn, we modeled the planets as circular disks with constant brightness temperature (Lin et al. 2009). The 3 mm brightness temperatures we adopted are 171.8 ± 1.7 K for Jupiter (Page et al. 2003; Griffin et al. 1986) and 149.3 ± 4.1 K for Saturn (Ulich 1981). Since the synthesized beam of AMiBA-13 is only a few times larger than the angular size of Jupiter or Saturn, the planets are slightly resolved. In the extreme case when Jupiter's size is close to $40''$, the longest baselines will detect about 15% less flux as compared to a point-source assumption. In addition, we included the obscuration effect of Saturn's rings as a function of their Earth-opening angle following the WMAP-derived model parameters (Weiland et al. 2011). Figure 9 shows this correction factor compared to a simple disk model of Saturn over the entire observing period from 2011 to 2014. The angular sizes of Jupiter and Saturn and the Earth-opening angle of Saturn's rings are calculated with the Python package 'PyEphem'[11].

4.4. *Noise Performance and Observing Efficiency*

Following Lin et al. (2009), we characterize the instrumental efficiency of AMiBA-13 by examining the net sensitivity as a function of the effective integration time. Here, the sensitivity is defined as the observed rms fluctuation of a cleaned map excluding the source region. The effective integration time sums up the integration of all valid (unflagged) visibility channels, accounting for the effects of relative weighting. Specifically, the effective integration time is defined as $t_{\rm eff} \equiv [(\sum_i w_i)^2 / \sum_i w_i^2]\, t_{\rm on_src}$, where $t_{\rm on_src}$ is the physical on-source time, w_i is the weight of each visibility, and the index i runs over all visibility elements. For AMiBA-13, in the ideal case of all instruments working and having identical weighting, the effective integration time and on-source time are related by $t_{\rm eff}^{\rm ideal}/t_{\rm on_src} = (78\ \text{baselines}) \times (2\ \text{polarizations}) \times (2\ \text{channels}) = 312$.

As an example, Figure 10 shows how the sensitivity depends on the effective integration time for our observations of

[11] http://rhodesmill.org/pyephem/

Table 4
Clusters Detected By AMiBA-13

Cluster	R.A. (J2000)	decl. (J2000)	Redshift	Sample [a]	Cool-Core [b]	Disturbed [b]
Abell 1689	13:11:29.45	-01:20:28.1	0.183	A	...	...
Abell 2163	16:15:46.20	-06:08:51.3	0.203	A	...	...
Abell 209	01:31:52.57	-13:36:38.8	0.206	C		
Abell 2261	17:22:27.25	+32:07:58.6	0.224	A,C	$\surd$	
MACS J1115.9+0129	11:15:52.05	+01:29:56.6	0.352	C	$\surd$	
RCS J1447+0828	14:47:26.89	+08:28:17.5	0.38	A,R	$\surd$	
MACS J1206.2-0847	12:06:12.28	-08:48:02.4	0.440	C		
MACS J0329.7-0211	03:29:41.68	-02:11:47.7	0.450	C	$\surd$	$\surd$
RX J1347.5-1145	13:47:30.59	-11:45:10.1	0.451	C	$\surd$	$\surd$
MACS J0717.5+3745	07:17:31.65	+37:45:18.5	0.548	C		$\surd$
MACS J2129.4-0741	21:29:26.06	-07:41:28.0	0.570	C	$\surd$	
RCS J2327-0204	23:27:26.16	-02:04:01.2	0.700	R	...	...

[a] A: AMiBA-7; C: CLASH; R: RCS
[b] X-ray morphology classification taken from Table 3 of Sayers et al. (2013). We additionally identify RCS J1447.5+0828 as a cool-core cluster on the basis of Hicks et al. (2013). Although RX J1347.5-1145 was not identified as a disturbed cluster in Sayers et al. (2013), significant substructure and large ellipticity were found for this cluster (see e.g. Postman et al. 2012).

Table 5
Integration Times and Detection Significance

Cluster	Obs. Time (hr)	Used Time (hr)	Eff. Time (hr)	Peak[a] (mJy/b)	Noise (mJy/b)	S/N[a]
Abell 1689	27.7	14.8	7.3	-46.1	4.0	11.5
Abell 2163	48.7	34.5	9.5	-28.1	3.9	7.3
Abell 209	14.4	2.7	0.8	-29.4	6.6	4.4
Abell 2261	22.4	11.8	4.4	-26.3	4.3	6.1
MACS J1115.9+0129	35.7	22.9	5.8	-25.8	3.1	8.4
RCS J1447+0828	9.5	2.6	0.7	-45.8	6.9	6.6
MACS J1206.2-0847	25.1	17.6	5.0	-36.2	3.3	11.1
MACS J0329.7-0211	33.4	11.6	4.0	-19.8	4.2	4.8
RX J1347.5-1145	29.5	11.0	2.5	-44.1	5.7	7.8
MACS J0717.5+3745	23.9	18.0	5.1	-44.4	5.1	8.7
MACS J2129.4-0741	57.7	29.4	7.3	-21.9	3.8	5.7
RCS J2327-0204	36.0	20.6	3.0	-32.7	5.3	6.1
Sum	364.0	197.5	55.4			

Note. — "Eff. Time" is defined in Section 4.4, "Obs. Time" and "Used Time" are defined in Section 4.5.
[a] "Raw" peak in the cleaned image, before applying the upward-flux correction.

Abell 1689. In this plot, visibilities are successively multiplied by $(-1)^j$, where j is the index of a data point, so that the signals of the cluster SZE or any other sources are significantly suppressed. The figure demonstrates that the variance of noise scales with the inverse of the effective integration time. Changing the multiplying factor from $(-1)^j$ to $\exp(i2\pi j/3)$, which cancels the signal for every three integrations, does not change the results.

The amplitude of the noise scaling curve can further be used to determine the overall efficiency η of the array. For AMiBA-13, we obtain $\eta = 0.4$, which is comparable to that of the AMiBA-7 system (Lin et al. 2009). We note, however, that as the efficiency is defined against the effective integration time, which is insensitive to data with a higher noise level, this overall efficiency only reflects particular baselines that have higher signal-to-noise ratios. Instead, the ratio between the used (unflagged) integration and the effective integration quantifies the array performance. This ratio ("Eff. Time" over "Used Time" in Table 5) varies from 14% to 49% and averages to 28% for the set of clusters shown in Table 5. This rather small average ratio indicates that a significant fraction of the correlations is much noisier than the rest of the array.

The root cause of the low-efficiency problem is that there are only four delay samples in the correlator, giving two highly coupled output channels. As geometric delays vary (due to, e.g., platform deformation), the leakage between the two output channels can change drastically. The ratio of the recovered power of the two channels from a flat-spectrum source ideally should be one. In practice, however, it can often reach five or more. When this happens in calibration, the suppressed channel can be identified from its magnified noise variance. Moreover, when the power imbalance between the channels is severe, the phase error is also amplified. This phase error affects both the suppressed and the enhanced channels. Therefore, it is better to downweight the correlator that is affected by a strong imbalance in order to reduce potential phase errors. Hence, we use the sum of the variances of both channels for the inverse-variance weighting (see also Section 3.5).

Typically, the sensitivity of our individual cluster observations reaches a level of 3 to 6 mJy beam^{-1}. Here, we further investigate whether any significant systematics are present below this limit. We do this by stacking data of many clusters together. The left panel in Figure 11 shows the stacked noise level as a function of the effective integration time for our sample of the twelve selected clusters (Table 4). This scaling is obtained by suppressing the cluster signal through phase scrambling. This test consistently confirms that the noise scal-

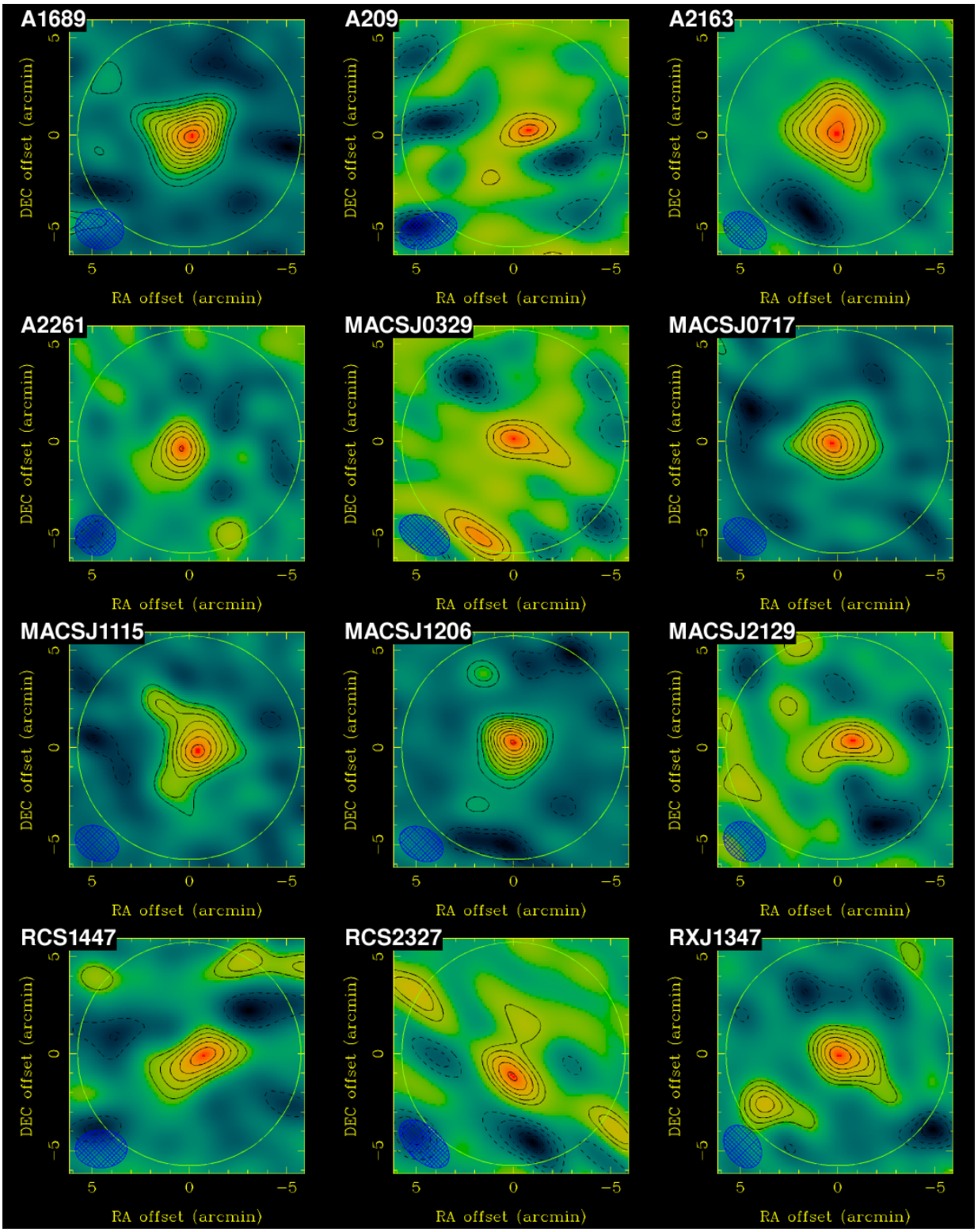

Figure 8. Cleaned AMiBA-13 images of the twelve cluster targets listed in Table 4. The contour levels are shown in units of σ, starting from the 2σ detection significance level. For each cluster, a solid circle indicates the FWHM of the primary beam ($11'$). The synthesized beam is displayed with a blue-shaded ellipse in the bottom-left corner.

ing holds down to a level slightly below 2 mJy beam^{-1}. The right panel in Figure 11 displays the stacked noise visibilities as a function of uv-distance, shown separately for the real and imaginary components. Here, the error bars indicate the expected level of uncertainty, $\sqrt{\langle\sigma^2\rangle}$, assuming Gaussian random noise, where $\langle\sigma^2\rangle = (\sum_i w_i^2\sigma_i^2)/(\sum_i w_i^2)$. The figure displays a noise level that is consistent with zero, demonstrating that no significant systematics are present.

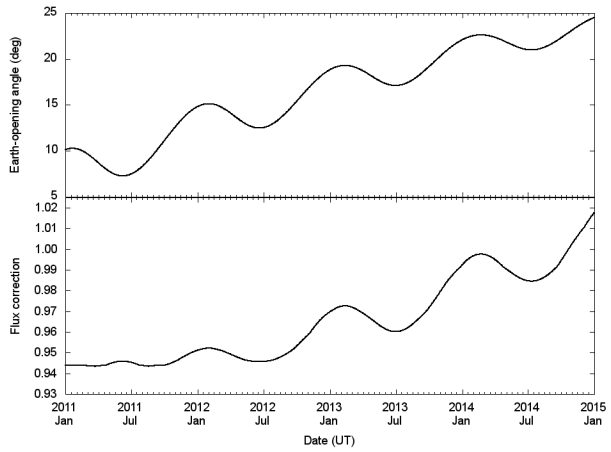

Figure 9. Top panel: Earth-opening angle of Saturn's rings during the observing period of 2011 to 2014. Bottom panel: corresponding correction factor for Saturn's flux, relative to a simple disk without rings.

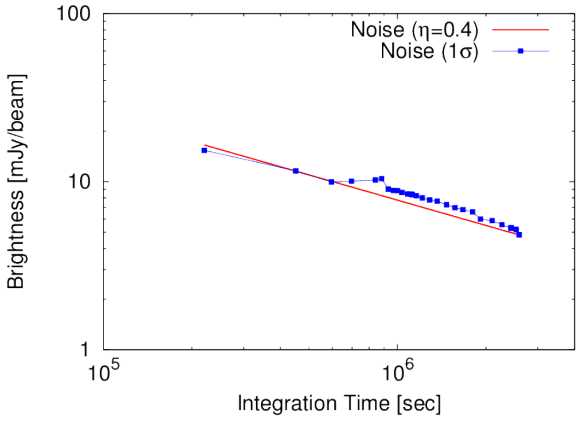

Figure 10. Sensitivity (rms noise) as a function of effective integration time for observations of A1689.

4.5. *Data Flagging*

Two integration times are listed for each cluster in Table 5. The "Obs. Time" shows the on-source integration on each cluster. The actual time spent on the observation is approximately double this value because of the trailing patch observing strategy. The "Used Time" shows the remaining integration time after flagging. Table 6 summarizes the fraction of data flagged by various criteria. "Offline" indicates the fraction of data flagged due to hardware malfunctions (including receivers and correlators). "High noise" sets a limit on the minimum weighting required to be included in the analysis. While including lowly weighed data does not affect the result, we choose to explicitly flag them out to help keep track of the problem. "Unstable BL" and "U/L band diff." are related to the varying delay and band-smearing issue of the broadband analog correlator. As mentioned in Section 3.1, the platform deformation can introduce an additional delay to baselines with already large instrumental delays and cause the visibility to be very sensitive to the combined delay. Its symptom reveals itself as unstable measurements in one-hour planet trackings and also as inconsistent phase/delay measurements between the upper and lower band. Therefore, we set up these criteria to flag them out. "Non-Gauss" catches the occasional glitches in the system that fail a Gaussianity test. Finally, "Cal. flag" indicates the fraction of data that are flagged as a consequence of flagged calibrator events. Overall, 30% to 50% of the data in the AMiBA-13 observations are flagged.

5. DISCUSSION

5.1. *Point Source Contamination*

AMiBA aims at measuring the cluster SZE with a single frequency band and only with a compact array. Without outrigger baselines to look for and subtract off point sources in both our target and trailing fields, the AMiBA measurements can potentially be contaminated. On the other hand, the choice of 90 GHz as the observing frequency is to avoid as much as possible the synchrotron sources at lower and the dusty sources at higher frequencies. Following Liu et al. (2010), we estimate the contamination from radio sources by extrapolating flux densities from low-frequency catalogs to 94 GHz, assuming a simple power law spectrum. Potential sources are identified from within an $11'$ radius (twice the FWHM of the primary beam) of both the target and trailing fields in the NVSS (1.4 GHz, Condon et al. 1998), PMN (4.85 GHz, Griffith et al. 1995), and GB6 (4.85 GHz, Gregory et al. 1996) catalogs. If a source is identified in both the 1.4 GHz and the 4.85 GHz catalogs, a spectral index is derived and used to estimate its 94 GHz flux density. If a source is detected in only one of the frequency bands, then we perform a Monte Carlo simulation with the spectral indices drawn from the five-year WMAP point source catalog (Wright et al. 2009). In particular, if a source is selected from the NVSS catalog but is not detected in the PMN or GB6 catalog, we limit the spectral index so that its flux density does not exceed the detection criteria of the 4.85 GHz surveys. For the twelve clusters shown in this work, no significant radio source with an extrapolated flux of more than 1 mJy at 90 GHz is found within our searching radius of both the target and the trailing fields.

5.2. *Interpreting Cluster Results*

One application of AMiBA measurements is to constrain gas pressure distributions in clusters. In this work, we adopt the spherical generalized Navarro–Frenk–White (gNFW) parametric form, first proposed by Nagai et al. (2007), to describe the gas pressure profile:

$$\mathbb{P}(x) = \frac{P(x)}{P_{500}} = \frac{P_0}{(c_{500}x)^\gamma \left[1 + (c_{500}x)^\alpha\right]^{(\beta-\gamma)/\alpha}}, \quad (6)$$

where $\mathbb{P}(x)$ is the dimensionless form of $P(x)$ that describes the shape of the profile with the scaled radius $x = r/R_{500}$ and $c_{500} = R_{500}/r_{gs}$, the ratio of R_{500}[12] to the gas characteristic radius r_{gs};[13] P_0 is the deviation from the characteristic pressure P_{500}, which is governed by gravity in the self-similar model. The AMiBA measurement is used to determine P_0 and r_{gs} (or equivalently c_{500}), while the slope parameters (α, β, γ) are fixed at the best-fit values found by Arnaud et al. (2010, A10, hereafter). If a cluster is classified as cool-core or disturbed (Table 4), the corresponding best-fit values from A10

[12] R_{500} or R_{500c} denotes the radius within which the enclosed mass is 500 times the critical density of the universe at the given redshift. Thus, M_{500} refers to the enclosed mass within R_{500}.

[13] The gas characteristic radius r_{gs} is independent of the dark matter characteristic radius r_s conventionally used in the NFW model.

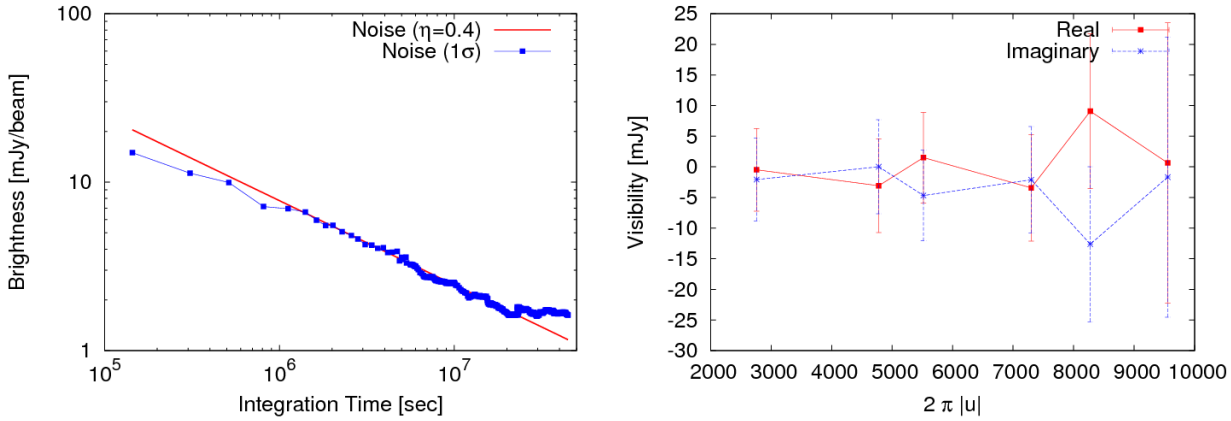

Figure 11. Stacked noise properties of AMiBA-13 observations for twelve selected clusters (Section 4.4). Left panel: stacked rms noise level as a function of effective integration time. Right panel: stacked noise visibilities as a function of uv-distance.

Table 6
Summary of Flags for Each Cluster in Percentage

Cluster	Offline	High noise	Unstable BL	U/L band diff.	Non-Gauss	Cal. flag	Used data
Abell 1689	7.6	12.4	15.2	1.1	0.8	9.5	53.6
Abell 2163	7.7	10.8	3.9	0.4	0.3	4.2	72.7
Abell 209	31.7	4.2	6.2	1.9	0.1	37.4	18.5
Abell 2261	4.3	14.7	9.9	0.3	0.2	17.7	52.8
MACS J1115.9+0129	21.4	8.8	2.5	0.1	0.4	2.6	64.3
RCS J1447+0828	22.0	5.1	5.0	2.7	0.5	37.4	27.4
MACS J1206.2-0847	10.5	7.3	5.5	0.5	0.2	6.0	70.1
MACS J0329.7-0211	17.4	11.1	4.1	1.5	0.2	31.0	34.8
RX J1347.5-1145	43.4	8.1	10.2	0.3	0.5	0.3	37.2
MACS J0717.5+3745	4.5	9.7	4.8	0.1	0.5	5.1	75.4
MACS J2129.4-0741	27.7	13.4	2.2	0.4	0.5	4.7	51.1
RCS J2327-02024	20.3	13.5	6.3	1.0	0.4	1.3	57.3

Note. — Individual flags are discussed in detail in Section 4.5.

is used. Otherwise, the best-fit values from the overall sample are used. R_{500} is obtained separately from the literature (X-ray or lensing) for each cluster.

Our data analysis is performed in two steps. The first step is to reconstruct the cluster visibility and remove any residual pointing offsets from the measurement. For this, we assume the cluster to be axisymmetric. Therefore, the AMiBA-13 data can be modeled with twelve independent real-valued band powers, $V(|u|)$, coming from six discrete baseline lengths with two spectral channels each, and with two more parameters for the pointing offsets. These parameters are then determined from the two-dimensional visibility data using a Markov Chain Monte Carlo (MCMC) method. After obtaining the visibility band powers, the second step is to fit the gNFW profile. A separate MCMC program is used for the profile fitting. Primary beam attenuation is applied to the model in this process before comparing to the band powers. The method is detailed in Wang et al. (*in preparation*). In Section 5.3 we demonstrate and apply this method to Abell 1689. For optically selected clusters, individual R_{500} estimates may be unavailable or unreliable due to large scatter. In this case, AMiBA SZE data can serve as a mass-proxy. We demonstrate this in Section 5.4 with the first targeted SZE detection of the cluster RCS J1447+0828.

5.3. *Combined AMiBA-7 and AMiBA-13 Observations of Abell 1689*

The rich cluster Abell 1689 at $z = 0.183$ is among the most powerful cosmic lenses known to date (Broadhurst et al. 2005; Oguri et al. 2005; Limousin et al. 2007; Umetsu & Broadhurst 2008; Coe et al. 2010; Diego et al. 2015), exhibiting a high degree of mass concentration in projection of the cluster. As such, the cluster has been a subject of detailed multiwavelength analyses (Lemze et al. 2009; Peng et al. 2009; Molnar et al. 2010a; Kawaharada et al. 2010; Morandi et al. 2011; Sereno et al. 2013; Okabe et al. 2014; Umetsu et al. 2015), and is one of the six clusters observed by AMiBA-7. A recent Bayesian analysis of the cluster (Umetsu et al. 2015) shows that combined multiwavelength data favor a triaxial geometry with minor-major axis ratio 0.39 ± 0.15 and major axis closely aligned with the line of sight ($22^\circ \pm 10^\circ$). This aligned orientation boosts the projected surface mass density of a massive cluster with $M_{200} = (1.7 \pm 0.3) \times 10^{15} M_\odot$ (Umetsu et al. 2015), and thus explains the exceptionally high lensing efficiency of the cluster.

Being massive and at a relatively low redshift, the bulk of the SZE signal is beyond the angular scales probed by AMiBA-13 but is largely captured by AMiBA-7. Hence, the cluster is well-suited for an examination of how well AMiBA can constrain the cluster pressure profile combining both the AMiBA-7 and AMiBA-13 data. Figure 12 shows the two overlaid SZE maps of the cluster observed with the two configurations of AMiBA.

We characterize the gas pressure structure of Abell 1689

Table 7
gNFW Parameters Determined for Abell 1689

Profile Name	P_0	c_{500}	α	β	γ	χ^{2a}
AMiBA	15.64	1.404	**1.051**[b]	**5.4905**[b]	**0.3081**[b]	28
A10 (individual)	23.13	1.16	0.78	**5.4905**[b]	0.399	40
A10 (universal)	8.403	1.177	1.051	**5.4905**[b]	0.3081	84
Planck	33.95	1.76	0.77	4.49	**0.31**[b]	57

[a] The χ^2 are computed against 18 AMiBA reconstructed band powers.
[b] The bold-faced numbers are fixed in their respective fitting.

with the gNFW profile (Equation 6). For profile fitting, we have fixed the following structural/shape parameters with the *universal* values given in Eq. (12) of A10:

$$[\gamma, \alpha, \beta] = [0.3081, 1.0510, 5.4905]. \quad (7)$$

We adopt $R_{500} = 1.351$ Mpc, given in Table C.1 of A10, which is based on an iterative estimation from their *XMM-Newton* data using the integrated mass vs integrated Compton-y, M_{500}–Y_X, scaling relation. We apply the flux-loss correction discussed in Section 3.5. The resulting AMiBA visibility band powers for Abell 1689 are shown in Figure 13. Our best-fit gNFW profile and its 1σ uncertainty range are also presented in Figure 13. For comparison, three additional gNFW pressure profiles determined for Abell 1689 from the literature are reproduced in the same plot. The first profile (marked A10 individual) is the best fit to the X-ray data of Abell 1689 in A10. The second profile (marked A10 universal) is the best fit to the X-ray data of the entire sample of 33 clusters in A10. In both cases, all parameters were free except for the outer slope parameter, $\beta = 5.4905$. The third profile is from Planck Collaboration et al. (2013), where they combined their *Planck* SZE data with archival *XMM-Newton* X-ray data (Planck Collaboration et al. 2011b) and fitted a gNFW profile. In their fitting, γ was fixed to 0.31, while the remaining parameters were free. In reproducing these profiles, $R_{500} = 1.351$ Mpc and the corresponding $P_{500} = 4.169 \times 10^3$ keV cm^{-3} were used. The profiles are multiplied by a Gaussian with a width of $11'.5$ to account for the AMiBA-13 primary beam effect and then inverted to uv-space for plotting. Table 7 summarizes the gNFW parameters of these profiles and their χ^2 values against the AMiBA data.

Abell 1689 has also been observed by other interferometers operating at 30 GHz, namely the Berkeley-Illinois-Maryland Array (BIMA), the Owens Valley Radio Observatory (OVRO), and the Sunyaev-Zel'dovich Array (SZA). The BIMA and OVRO observations are presented in LaRoque et al. (2006), while the SZA observations are presented in Gralla et al. (2011). Umetsu et al. (2015) determined the best-fit gNFW pressure parameters from the BIMA/OVRO and SZA data separately. The gNFW models were then cylindrically integrated to yield $Y(< r)$ at integration radii r probed by the respective instruments. These results are summarized in their Table 6. Umetsu et al. (2015) also determined $Y(< 13')$ from *Planck* SZE observations. Figure 14 compares the cylindrically integrated $Y(< r)$ measurements from AMiBA and other SZE observations. After applying the upward-flux correction, we find that the AMiBA results are in agreement with both the SZA and the BIMA/OVRO results. At larger integration radii, the AMiBA constraints are weaker because of the shallow AMiBA-7 data. The AMiBA results are consistent within a 1σ uncertainty with the *Planck* results. Further discussion on the gNFW profile fitting and integrated Compton-y results for the other clusters in our sample will be presented in a forthcoming paper (Wang et al., in preparation).

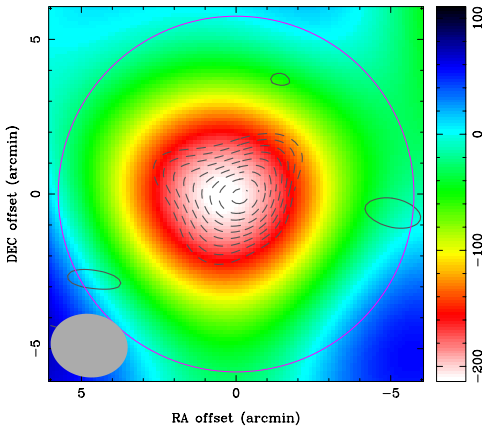

Figure 12. AMiBA SZE maps of the cluster Abell 1689. The image is $12' \times 12'$ in size and centered on the cluster center (Table 4). The color image shows the AMiBA-7 observations (Wu et al. 2009) of the cluster with an rms noise level of 40 mJy per AMiBA-7 synthesized beam, that is approximately circular with a FWHM of $6.5'$. The black contours show the AMiBA-13 observations. The contour levels are shown in units of σ and start at $\pm 3\sigma$ for positive (solid) and negative (dashed) flux levels, respectively, where 1σ is about 4 mJy per beam. The synthesized beam of AMiBA-13 is indicated by a gray-shaded ellipse in the lower-left corner.

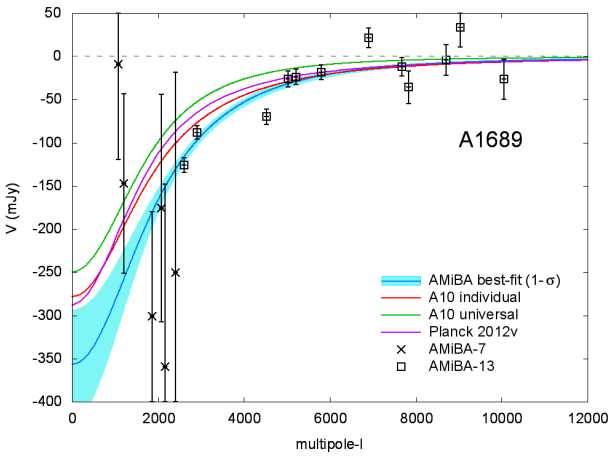

Figure 13. Visibility flux profile of Abell 1689 as a function of angular multipole l. The black crosses and squares with error bars represent visibility band powers obtained from AMiBA-7 ($l < 2400$) and AMiBA-13 ($l > 2400$) observations, respectively. The blue-shaded region shows the 68.3% confidence interval in the marginalized posterior distribution of the gNFW pressure profile. Abell 1689 (see Table C.1 of A10, RXC J1311.4−0120 aka Abell 1689). The green line represents the A10 *universal* gNFW profile. The purple line represents the gNFW profile for the cluster obtained by Planck Collaboration et al. (2013) from *Planck* SZ + *XMM-Newton* observations. All model predictions are multiplied with a Gaussian with a width of $11'.5$ in image domain to account for the primary beam attenuation of AMiBA-13.

5.4. *SZE Detection of the Cluster RCS J1447+0828*

In this section we explore the possibility of using AMiBA SZE observations as a proxy for the total mass of clusters. The

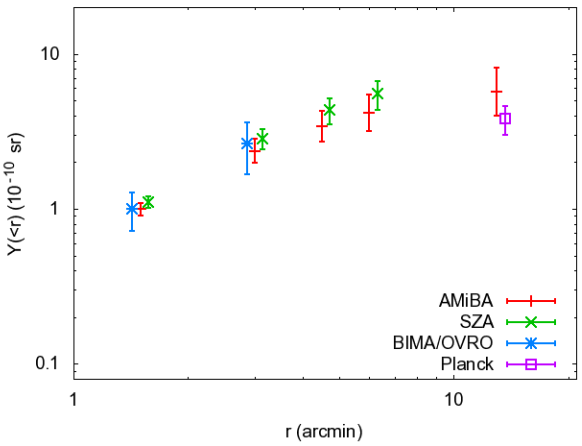

Figure 14. Multi-scale SZE constraints on the cylindrically integrated Compton-y, $Y(< r)$, derived for Abell 1689. Our joint AMiBA-7 and AMiBA-13 constraints (red) are compared with other interferometric (BIMA/OVRO: blue; SZA: green) and bolometric (*Planck*: purple) SZE observations. For visual clarity, results measured at the same enclosing radius are slightly shifted from each other horizontally. The AMiBA results, after the upward-flux correction (see Section 3.5), are consistent with all other SZE observations. The AMiBA uncertainty increases with increasing integration radius (r), showing that the pressure structure on larger angular scales is poorly constrained by AMiBA.

primary AMiBA SZE observable considered here is the peak flux density $I_{\rm SZ}$ in a dirty image, constructed from visiblity data with natural weighting. This is a direct observable from interferometric AMiBA observations and is closely related to $Y_{2500} = Y(< R_{2500})$, the integrated Compton-y parameter interior to a cylinder of radius R_{2500}. In Appendix A we describe our Monte–Carlo method that simulates the probability distribution $P(I_{\rm SZ}|M_{200})$ of the AMiBA SZE observable as a function of halo mass M_{200} (and redshift), given the underlying halo concentration–mass (c–M) relation and intrinsic distributions of the gNFW pressure profile parameters.

As a demonstration, we choose RCS J1447+0828, an optically selected cluster at $z = 0.38$ from the Red-sequence Cluster Survey (Gladders & Yee 2005, RCS). Subsequent *Chandra* X-ray observations identified it as a strong cool-core cluster (Hicks et al. 2013). Figure 15 shows the $I_{\rm SZ}$–M_{200} relation predicted for this cluster, with the simulated gNFW parameters drawn from the REXCESS cool-core subsample presented in A10 (see Appendix A). Also shown in this figure is the Y_{2500}–M_{200} relation obtained using the same prior for comparison. The slope of $\log_{10} I_{\rm SZ}$ versus $\log_{10} M_{200}$ is 1.21 with a scatter of ± 0.13 dex. The slope of $\log_{10} Y_{2500}$ versus $\log_{10} M_{200}$ is 1.73 with a scatter of ± 0.14 dex. While Y_{2500} is calculated from the simulated intrinsic cluster profile, the observable $I_{\rm SZ}$ is obtained after applying a Gaussian beam with a FWHM of $11\farcm5$ to simulate the primary beam attenuation of AMiBA-13 observations.

Multiplying the probability distribution function $P(I_{\rm SZ}|M_{200})$ with a Gaussian likelihood of the AMiBA-13 measurement $I_{\rm SZ} = -57.3 \pm 7.3\,{\rm mJy\,beam^{-1}}$ (Table 5, after the upward-flux correction) and integrating over $I_{\rm SZ}$ yields the posterior distribution of M_{200} for RCS J1447+0828, as shown in Figure 16. Here, we take the biweight estimator of Beers et al. (1990) to be the central location ($C_{\rm BI}$) and scale ($S_{\rm BI}$) of the marginalized posterior mass distribution. We find $M_{200} = 26.9 \pm 7.4 \times 10^{14} M_\odot$. From the same simulation, we can also construct the mass relation at a higher overdensity, e.g., $I_{\rm SZ}$–M_{2500}. With the AMiBA-13 measurement, we find $M_{2500} = 6.6 \pm 2.1 \times 10^{14} M_\odot$. The latter result can be compared to the X-ray-based M_{2500} mass estimates of Hicks et al. (2013), who find from *Chandra* observations $M_{2500} = 4.8^{+0.7}_{-0.5} \times 10^{14} M_\odot$ using $Y_{\rm X}$ as a mass proxy and $M_{2500} = (6 \pm 2) \times 10^{14} M_\odot$ using $T_{\rm X}$. The AMiBA-13 estimate of M_{2500} is consistent with these measurements within uncertainties.

Alternatively, one can relax the cool-core assumption and simulate the cluster observable using gNFW parameters drawn from the full REXCESS sample in A10. The posterior distribution of M_{200}, also shown in Figure 16, favors higher masses than the cool-core results: $M_{200} = 31.1 \pm 10.8 \times 10^{14} M_\odot$. At a higher overdensity, we obtain $M_{2500} = 7.4 \pm 2.5 \times 10^{14} M_\odot$. In general, for a given AMiBA-13 SZE measurement, the cool-core and disturbed cluster priors give lower and higher mass estimates, respectively, relative to those from the full-sample prior. The discrepancy is of the same order as the width of posterior mass distributions.

5.5. *Mass Estimates Compared to Lensing Masses*

In Section 5.4, we showed that, for the cluster RCS J1447+0828, the AMiBA-13 derived and X-ray based cluster mass estimates are consistent with each other. For the rest of the clusters shown in this work, a direct comparison with gravitational lensing mass measurements can be made.

Table 8 and Figure 17 summarize and compare, for the other eleven clusters, recent lensing mass measurements taken from the published literature and our AMiBA-13 results. The spherical enclosed masses are derived at two over-densities, M_{200} and M_{2500}. To derive $M^{\rm SZ}$ from AMiBA-13 data, we performed Monte-Carlo simulations for each cluster with gNFW parameters drawn from either the cool-core or disturbed subsamples, or the full sample of A10, according to the X-ray classification of the cluster (see Table 4 and Sayers et al. 2013). For clusters identified as both cool-core and disturbed (MACS J0329.7-0211 and RX J1347.5-1145), we make a less-informative assumption and simulate them with gNFW parameters drawn from the full sample range (see Section 5.4). Figure 17 shows that the three cool-core clusters tend to have lower $M^{\rm SZ}$ estimates with $M^{\rm GL}/M^{\rm SZ} > 1$. It hints, albeit with a small sample, that using the less informative full-sample prior, which includes the parameter ranges of cool-core and disturbed subsamples, may be adequate for cluster mass estimation. We also quote the geometric mean and uncertainty (e.g., Umetsu et al. 2016) of the mass ratio $\langle M^{\rm GL}/M^{\rm SZ}\rangle_g$, where each cluster is weighted by its error, and the errors of $M^{\rm SZ}$ and $M^{\rm GL}$ are treated as independent. The mean mass ratio of this sample with eleven clusters shows no significant bias at both over-densities.

6. SUMMARY AND CONCLUSIONS

The Yuan-Tseh Lee Array for Microwave Background Anisotropy (AMiBA) is a co-planar interferometer array operating at a wavelength of 3 mm to measure the Sunyaev-Zeldovich effect (SZE) of galaxy clusters at arcminute scales. After an intial phase with seven close-packed 0.6 m antennas (AMiBA-7), the AMiBA was upgraded to a 13-element array. In the following, we summarize the AMiBA expansion, its commissioning and results from its SZE observing program.

- *Array upgrade.* The expanded AMiBA-13 is comprised of thirteen new lightweight carbon-fiber-reinforced

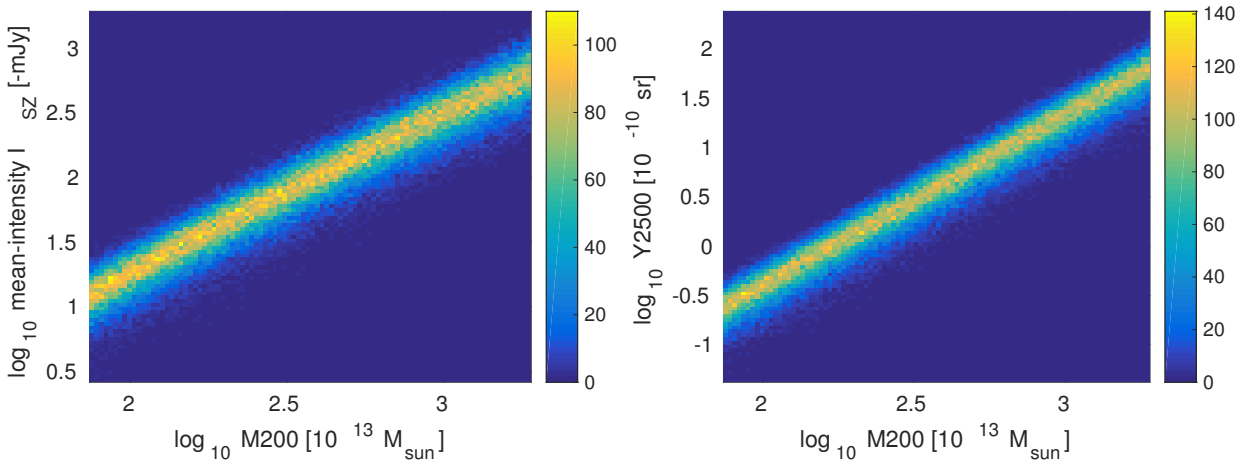

Figure 15. Simulated scaling relations for RCS J1447+0828 assuming that it is a cool-core cluster (see Section 5.4). **Left:** $I_{\rm SZ} - M_{200}$ relation. **Right:** $Y_{2500} - M_{200}$ relation. A fixed number of clusters were simulated in each of the logarithmically spaced mass bin. The color scale depicts the number of clusters falling in the logarithmically spaced $I_{\rm SZ}$ or Y_{2500} cells at a given mass bin.

Table 8
Comparison of Mass Estimates with Lensing

Cluster	sim. type[a]	$M_{200}^{\rm SZ}$ $10^{14}M_\odot$	$M_{200}^{\rm GL}$ [b] $10^{14}M_\odot$	$M_{2500}^{\rm SZ}$ $10^{14}M_\odot$	$M_{2500}^{\rm GL}$ [b] $10^{14}M_\odot$	Lensing ref.
Abell 1689	f	43.3 ± 22.1	19.8 ± 1.4	10.4 ± 5.2	8.7 ± 0.65	Umetsu et al. (2015)
Abell 2163	f	24.0 ± 9.2	28.2 ± 5.3	6.0 ± 2.3	4.4 ± 0.75	Okabe et al. (2011)
Abell 209	f	25.3 ± 11.7	16.1 ± 3.6	6.4 ± 2.9	3.1 ± 0.71	Umetsu et al. (2016)
Abell 2261	c	17.6 ± 5.6	24.1 ± 5.4	4.6 ± 1.5	6.2 ± 1.08	Umetsu et al. (2016)
MACS J1115.9+0129	c	17.1 ± 4.6	17.4 ± 4.0	4.4 ± 1.3	3.7 ± 0.86	Umetsu et al. (2016)
MACS J1206.2-0847	f	24.7 ± 7.3	19.0 ± 4.4	6.0 ± 2.1	4.8 ± 1.06	Umetsu et al. (2016)
MACS J0329.7-0211	f[c]	14.9 ± 4.5	9.4 ± 2.1	3.7 ± 1.2	3.4 ± 0.67	Umetsu et al. (2016)
RX J1347.5-1145	f[c]	29.1 ± 9.6	35.8 ± 9.2	6.9 ± 2.4	8.0 ± 1.70	Umetsu et al. (2016)
MACS J0717.5+3745	d	33.2 ± 10.3	28.0 ± 5.6	7.6 ± 2.5	3.6 ± 0.91	Umetsu et al. (2016)
MACS J2129.4-0741	c	15.0 ± 4.2	20.4 ± 5.9	3.7 ± 1.1	5.6 ± 2.82	Applegate et al. (2014)[d]
RCS J2327-0204	f	20.3 ± 5.7	20.9 ± 8.4	4.8 ± 1.5	4.5 ± 1.25	Sharon et al. (2015)
$\langle M^{\rm GL}/M^{\rm SZ}\rangle_g$		0.93 ± 0.12		0.86 ± 0.11		

[a] gNFW parameter range for the Monte-Carlo simulations. f: full sample in A10; c: cool-core clusters subsample; d: disturbed clusters subsample.
[b] Lensing masses have been converted to the cosmology adopted in this work, where $h = 0.67$.
[c] For clusters that are classified as both cool-core and disturbed, we choose to use a less-informative prior by drawing simulation parameters from the full sample in A10.
[d] The authors obtained a spherical mass estimate of $M(< 1.5\,{\rm Mpc})$ for MACS J2129.4-0741 assuming the NFW model with halo concentration $c_{200} = 4$. We have converted it to the spherical M_{200} and M_{2500} masses using the same NFW model.

plastic (CFRP) 1.2 m diameter antennas with a field-of-view (FoV) of $11'$. Despite weighing only 25 kg, the antennas show excellent structural behaviour with an overall aperture efficiency of about 0.6. All antennas are co-mounted on the hexapod-driven CFRP platform in a close-packed configuration, yielding baselines from 1.4 m to 4.8 m which sample scales on the sky from $2'$ to $10'$ with a synthesized beam of $2\farcm5$. The shortest baseline of 1.4 m is chosen to minimize both CMB leakage ($\sim$ 11 mJy) and antenna cross-talk (~ -135 dB). Additional correlators and six new receivers with noise temperatures between 55-75 K complete the AMiBA expansion.

- *Commissioning and new correction schemes.* For a bandwidth of 20 GHz, baselines of up to 5 m and an antenna FoV of $11'$, instrumental delays need to be within about ± 22 ps for AMiBA-13. Delays are initially measured for every baseline with a movable broadband noise source emitting towards the two receivers, and then further iterated by scanning the Sun with the entire array. Optimized delay solutions for all 78 baselines show an rms scatter of 22 ps in residual delays. Additional pointing-dependent geometrical delays can result from the platform deformation. This repeatable deformation – entirely negligible for the earlier central close-packed AMiBA-7 – is modelled both from extensive photogrammetry surveys and the all-sky pointing correlation between two optical telescopes mounted on two different locations on the platform. This yields an all-sky deformation model. Platform deformation-induced antenna misalignments are measured to be within $\pm 2'$, leading to an efficiency loss of a few percent. The refined all-sky radio pointing error is about $0\farcm4$ in rms, with a repeatability around $10''$, which gives an efficiency loss of less than 2%. Overall, platform- and pointing-induced phase errors can reduce the point source flux recovery by 15% to 25%. Measured visibilities are, thus, upward corrected by a factor of 1.25

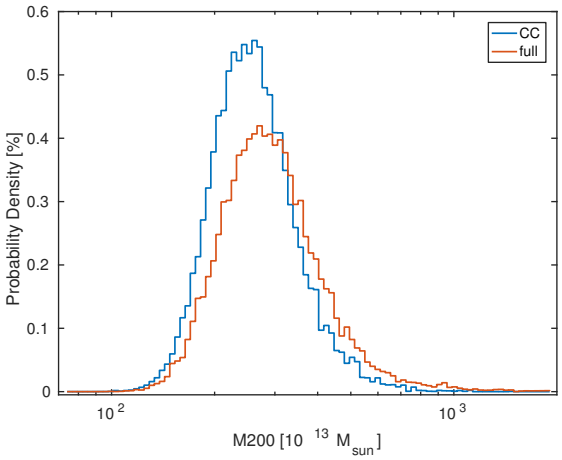

Figure 16. Posterior mass distribution of RCS J1447+0828 derived from the $I_{\rm SZ} - M_{200}$ scaling relation, given the AMiBA-13 measured peak intensity $I_{\rm SZ} = -57.3 \pm 7.3\,{\rm mJy\,beam^{-1}}$. The blue curve is derived from the cool-core (CC) cluster simulation shown in the left panel of Figure 15. The red curve shows the posterior mass distribution similarly derived from the full cluster sample simulation (see text).

to account for phase decoherence. An additional $\pm 5\%$ systematic uncertainty is added in quadrature to the statistical errors.

- *Calibration, tests and array performance.* Flux and gain calibration are done by observing Jupiter and Saturn for at least one hour every night. Obscuration effects due to Saturn's rings are accounted for beyond a simple disk model. Data are flagged and checked against various criteria, such as, high noise, unstable baselines, upper-lower-band differences, non-Gaussianity, and calibration failure. Typically, 20% to 50% of the cluster data are flagged. We demonstrate the absence of further systematics with a noise level consistent with zero in stacked uv-visibilities. Scaling of stacked noise with integration time indicates an overall array efficiency $\eta = 0.4$.

- *Cluster SZE observing program.* Targeted cluster SZE observations with AMiBA-13 started in mid-2011 and ended in late 2014. Observations are carried out in a lead-trail observing mode. The AMiBA-13 cluster sample consists of (1) the six clusters observed with AMiBA-7, (2) twenty clusters selected from the Cluster Lensing And Supernova survey with Hubble (CLASH) with complementary strong- and weak-lensing, X-ray, and additional SZE data from Bolocam and MUSTANG, and (3) seven optically selected cluster candidates from the Red-sequence Cluster Survey 2 (RCS2). From these samples, we present maps of a subset of twelve clusters, in a redshift range from 0.183 to 0.700, with AMiBA-13 SZE detections with signal-to-noise ratios ranging from about 5 to 11. Achieved noise levels are between 3 to 7 mJy/beam. No significant radio point sources, with extrapolated flux levels of more than 1 mJy at 90 GHz, are found in the target or trailing fields.

- *AMiBA SZE detections of A1689 and RCS J1447.* AMiBA-7 and AMiBA-13 observations of Abell 1689 are combined and jointly fitted to a gNFW model. Our cylindrically integrated Compton-y values for five radii are consistent with BIMA/OVRO, SZA, and *Planck* results. We report the first targeted SZE detection towards the optically selected cluster RCS J1447+0828. We develop a Monte-Carlo approach to predict the AMiBA-13 observed SZE peak flux given an underlying halo concentration-mass relation and intrinsic distributions of gNFW pressure profile parameters. It is then used reversely to constrain halo mass given the AMiBA-13 SZE flux measurement. Our estimates yield $M_{200} = 26.9 \pm 7.4 \times 10^{14} M_\odot$ and $M_{2500} = 6.6 \pm 2.1 \times 10^{14} M_\odot$. The AMiBA-13 result for M_{2500} agrees with X-ray-based measurements within error bars.

- *AMiBA-13 derived total mass estimates versus lensing masses.* Using the same Monte-Carlo method, we have obtained total mass estimates for the other eleven clusters studied in this work and compared them with recent lensing mass measurements available in the literature. For this small sample, we find that the AMiBA-13 and lensing masses are in agreement. The geometric mean of the mass ratios is found to be $\langle M_{200}^{\rm GL}/M_{200}^{\rm SZ}\rangle_g = 0.93 \pm 0.12$ and $\langle M_{2500}^{\rm GL}/M_{2500}^{\rm SZ}\rangle_g = 0.86 \pm 0.11$.

Acknowledgments Capital and operational funding for AMiBA came from the Ministry of Education and the Ministry of Science and Technology of Taiwan (MoST) as part of the Cosmology and Particle Astrophysics (CosPA) initiative. Additional funding also came in the form of an Academia Sinica Key Project. We thank the Smithsonian Astrophysical Observatory for hosting the AMiBA project staff at the SMA Hilo Base Facility. We thank the NOAA for locating the AMiBA project on their site on Mauna Loa. We also thank the Hawaiian people for allowing astronomers to work on their mountains in order to study the universe. JHPW acknowledges support by the NSC grant NSC 100-2112-M-002-004-MY3 and the MoST grant MoST 103-2628-M-002-006-MY4 Support from the STFC for MB is also acknowledged. PMK acknowledges support from MoST 103-2119-M-001-009 and from an Academia Sinica Career Development Award. KU acknowledges support by the MoST grants MOST 103-2112-M-001-030-MY3 and MOST 103-2112-M-001-003-MY3. We are grateful to Nobuhiro Okabe for useful comments and help with the lensing mass comparison. We also thank the anonymous referee for their useful comments and suggestions.

REFERENCES

Agudo, I., Thum, C., Wiesemeyer, H., et al. 2012, A&A, 541, A111
Applegate, D. E., von der Linden, A., Kelly, P. L., et al. 2014, MNRAS, 439, 48
Arnaud, M., Pratt, G. W., Piffaretti, R., et al. 2010, A&A, 517, A92
Beers, T. C., Flynn, K., & Gebhardt, K. 1990, AJ, 100, 32
Birkinshaw, M. 1999, Phys. Rep., 310, 97
Bleem, L. E., Stalder, B., de Haan, T., et al. 2015, ApJS, 216, 27
Broadhurst, T., Benítez, N., Coe, D., et al. 2005, ApJ, 621, 53
Carlstrom, J. E., Holder, G. P., & Reese, E. D. 2002, ARA&A, 40, 643
Chen, M.-T., Li, C.-T., Hwang, Y.-J., et al. 2009, ApJ, 694, 1664
Coe, D., Benítez, N., Broadhurst, T., & Moustakas, L. A. 2010, ApJ, 723, 1678
Condon, J. J., Cotton, W. D., Greisen, E. W., et al. 1998, AJ, 115, 1693
Diego, J. M., Broadhurst, T., Benitez, N., et al. 2015, MNRAS, 446, 683
Donahue, M., Voit, G. M., Mahdavi, A., et al. 2014, ApJ, 794, 136
Dutton, A. A., & Macciò, A. V. 2014, MNRAS, 441, 3359
Gilbank, D. G., Gladders, M. D., Yee, H. K. C., & Hsieh, B. C. 2011, AJ, 141, 94

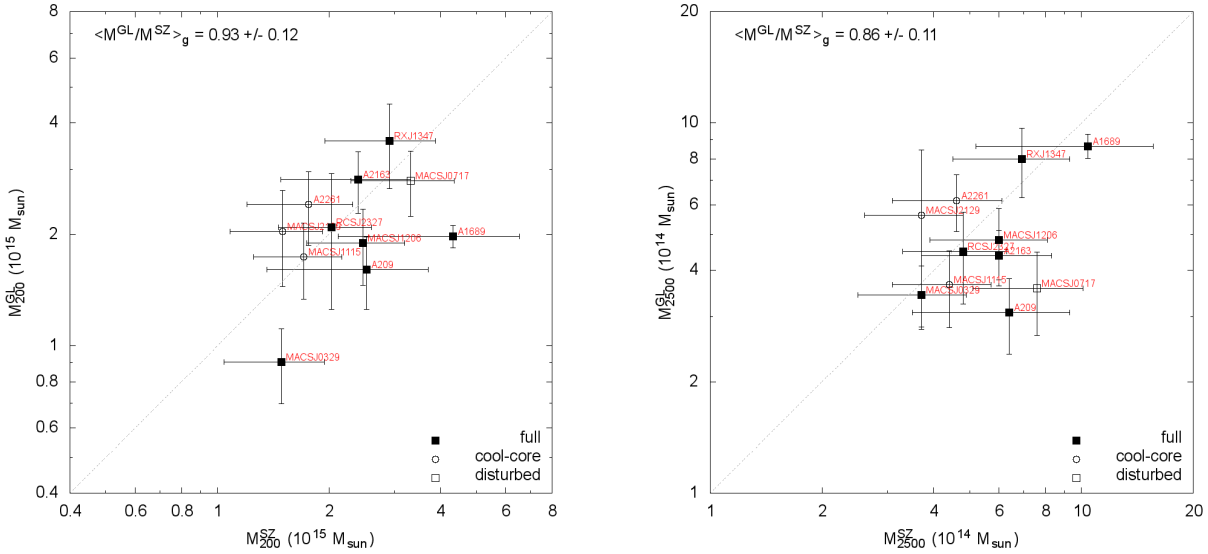

Figure 17. Comparison of gravitational lensing and AMiBA-13 SZ derived masses for eleven clusters in our sample. The spherical enclosed masses are derived at two overdensities, M_{200} (left) and M_{2500} (right). The one-to-one relation is represented by the dotted line. The geometric mean of the mass ratios is indicated at the top of each diagram.

Gladders, M. D., & Yee, H. K. C. 2005, ApJS, 157, 1
Gralla, M. B., Sharon, K., Gladders, M. D., et al. 2011, ApJ, 737, 74
Gregory, P. C., Scott, W. K., Douglas, K., & Condon, J. J. 1996, ApJS, 103, 427
Griffin, M. J., Ade, P. A. R., Orton, G. S., et al. 1986, Icarus, 65, 244
Griffith, M. R., Wright, A. E., Burke, B. F., & Ekers, R. D. 1995, ApJS, 97, 347
Hasselfield, M., Hilton, M., Marriage, T. A., et al. 2013, JCAP, 7, 008
Hicks, A. K., Pratt, G. W., Donahue, M., et al. 2013, MNRAS, 431, 2542
Hinshaw, G., Larson, D., Komatsu, E., et al. 2013, ApJS, 208, 19
Ho, P. T. P., Altamirano, P., Chang, C.-H., et al. 2009, ApJ, 694, 1610
Huang, C.-W. L., Wu, J.-H. P., Ho, P. T. P., et al. 2010, ApJ, 716, 758
Huang, Y.-D., Raffin, P., & Chen, M.-T. 2011, IEEE Transactions on Antennas and Propagation, 59, 2022
Huang, Y. D., Raffin, P., Chen, M.-T., Altamirano, P., & Oshiro, P. 2008, in Society of Photo-Optical Instrumentation Engineers (SPIE) Conference Series, Vol. 7012, Society of Photo-Optical Instrumentation Engineers (SPIE) Conference Series
Kawaharada, M., Okabe, N., Umetsu, K., et al. 2010, ApJ, 714, 423
Koch, P., Kesteven, M., Chang, Y.-Y., et al. 2008, in Society of Photo-Optical Instrumentation Engineers (SPIE) Conference Series, Vol. 7018, Society of Photo-Optical Instrumentation Engineers (SPIE) Conference Series
Koch, P. M., Kesteven, M., Nishioka, H., et al. 2009, ApJ, 694, 1670
Koch, P. M., Raffin, P., Huang, Y.-D., et al. 2011, PASP, 123, 198
LaRoque, S. J., Bonamente, M., Carlstrom, J. E., et al. 2006, ApJ, 652, 917
Lemze, D., Broadhurst, T., Rephaeli, Y., Barkana, R., & Umetsu, K. 2009, ApJ, 701, 1336
Li, C.-T., Kubo, D. Y., Wilson, W., et al. 2010, ApJ, 716, 746
Liao, Y.-W., Proty Wu, J.-H., Ho, P. T. P., et al. 2010, ApJ, 713, 584
Liao, Y.-W., Lin, K.-Y., Huang, Y.-D., et al. 2013, ApJ, 769, 71
Limousin, M., Richard, J., Jullo, E., et al. 2007, ApJ, 668, 643
Lin, K.-Y., Li, C.-T., Ho, P. T. P., et al. 2009, ApJ, 694, 1629
Liu, G.-C., Birkinshaw, M., Proty Wu, J.-H., et al. 2010, ApJ, 720, 608
Mason, B. S., Dicker, S. R., Korngut, P. M., et al. 2010, ApJ, 716, 739
Merten, J., Meneghetti, M., Postman, M., et al. 2015, ApJ, 806, 4
Molnar, S. M., Chiu, I.-N., Umetsu, K., et al. 2010a, ApJ, 724, L1
Molnar, S. M., Umetsu, K., Birkinshaw, M., et al. 2010b, ApJ, 723, 1272
Morandi, A., Limousin, M., Rephaeli, Y., et al. 2011, MNRAS, 416, 2567
Mroczkowski, T., Dicker, S., Sayers, J., et al. 2012, ApJ, 761, 47
Nagai, D., Kravtsov, A. V., & Vikhlinin, A. 2007, ApJ, 668, 1
Navarro, J. F., Frenk, C. S., & White, S. D. M. 1997, ApJ, 490, 493
Nishioka, H., Wang, F.-C., Wu, J.-H. P., et al. 2009, ApJ, 694, 1637
Oguri, M., Takada, M., Umetsu, K., & Broadhurst, T. 2005, ApJ, 632, 841
Okabe, N., Bourdin, H., Mazzotta, P., & Maurogordato, S. 2011, ApJ, 741, 116
Okabe, N., Umetsu, K., Tamura, T., et al. 2014, PASJ, 66, 99
Padin, S., Cartwright, J. K., Joy, M., & Meitzler, J. C. 2000, IEEE Transactions on Antennas and Propagation, 48, 836
Page, L., Barnes, C., Hinshaw, G., et al. 2003, ApJS, 148, 39
Peng, E.-H., Andersson, K., Bautz, M. W., & Garmire, G. P. 2009, ApJ, 701, 1283
Planck Collaboration, Aghanim, N., Arnaud, M., et al. 2011a, A&A, 536, A9
Planck Collaboration, Ade, P. A. R., Aghanim, N., et al. 2011b, A&A, 536, A11
—. 2013, A&A, 550, A131
—. 2014, A&A, 571, A16
—. 2015a, ArXiv e-prints, arXiv:1502.01589
—. 2015b, ArXiv e-prints, arXiv:1502.01598
Postman, M., Coe, D., Benítez, N., et al. 2012, ApJS, 199, 25
Raffin, P., Koch, P., Huang, Y.-D., et al. 2006, in Society of Photo-Optical Instrumentation Engineers (SPIE) Conference Series, Vol. 6273, Society of Photo-Optical Instrumentation Engineers (SPIE) Conference Series
Raffin, P. A., Martin, R. N., Huang, Y.-D., et al. 2004, in Society of Photo-Optical Instrumentation Engineers (SPIE) Conference Series, Vol. 5495, Society of Photo-Optical Instrumentation Engineers (SPIE) Conference Series, ed. J. Antebi & D. Lemke, 159
Ruze, J. 1966, IEEE Proceedings, 54, 633
Sayers, J., Czakon, N. G., Mantz, A., et al. 2013, ApJ, 768, 177
Sereno, M., Ettori, S., Umetsu, K., & Baldi, A. 2013, MNRAS, 428, 2241
Sharon, K., Gladders, M. D., Marrone, D. P., et al. 2015, ApJ, 814, 21
Sunyaev, R. A., & Zeldovich, Y. B. 1970, Comments on Astrophysics and Space Physics, 2, 66
—. 1972, Comments on Astrophysics and Space Physics, 4, 173
Ulich, B. L. 1981, AJ, 86, 1619
Umetsu, K., & Broadhurst, T. 2008, ApJ, 684, 177
Umetsu, K., Zitrin, A., Gruen, D., et al. 2016, ApJ, 821, 116
Umetsu, K., Birkinshaw, M., Liu, G.-C., et al. 2009, ApJ, 694, 1643
Umetsu, K., Medezinski, E., Nonino, M., et al. 2014, ApJ, 795, 163
Umetsu, K., Sereno, M., Medezinski, E., et al. 2015, ApJ, 806, 207
Weiland, J. L., Odegard, N., Hill, R. S., et al. 2011, ApJS, 192, 19
Wright, E. L., Chen, X., Odegard, N., et al. 2009, ApJS, 180, 283
Wu, J.-H. P., Ho, P. T. P., Huang, C.-W. L., et al. 2009, ApJ, 694, 1619
Zitrin, A., Fabris, A., Merten, J., et al. 2015, ApJ, 801, 44

APPENDIX

A. MONTE-CARLO SIMULATIONS FOR CLUSTER MASS ESTIMATES

The gNFW pressure profile in Equation (6) is indirectly related to the halo mass through P_{500}. With the mass dependence of P_{500} explicitly written out (see e.g., Nagai et al. 2007), the cluster physical pressure profile becomes

$$P(r) = 1.65 \times 10^{-3} h(z)^{8/3} \left[\frac{M_{500}}{3 \times 10^{14} h_{70}^{-1} M_\odot}\right]^{2/3+0.12} \times \mathbb{P}(x) h_{70}^2 \,\mathrm{keV\,cm^{-3}}\,, \tag{A1}$$

where $\mathcal{P}(\S)$ is defined in equation (6).

In the simulation here, we relate the cluster size R_{500} to its halo mass assuming an NFW model (Navarro et al. 1997) through a concentration – mass (c−M) relation from Dutton & Macciò (2014), with redshift evolution:

$$\begin{aligned} \log_{10} c_{200} &= a + b \log_{10}\left(M_{200}/\left[10^{12} h_0^{-1} M_\odot\right]\right)\,, \\ a &= 0.520 + (0.905 - 0.520)\exp(-0.617 z^{1.21})\,, \\ b &= -0.101 + 0.026 z\,. \end{aligned} \tag{A2}$$

We choose M_{200} to represent the virial mass. For each M_{200}, R_{500} and M_{500} were obtained from this c−M relation and then substituted in the pressure equation (A1).

At a given halo mass, Monte–Carlo (MC) simulations draw a set of gNFW parameters[14] (P_0, c_{500}, α, and γ) from the prior parameter distribution and calculates the desired observable. Here, we assume that (1) the gNFW parameters are independent of halo mass, and (2) the parameters fitted for individual clusters listed in Table C.1 of A10 are a fair representation of the intrinsic scatter of the parameters. Specifically, three of the parameters are modeled as Gaussian random numbers in logarithmic space ($\log_{10} P_0$, $\log_{10} c_{500}$, $\log_{10} \alpha$), while the remaining parameter (γ) is modeled as a Gaussian random number in linear space. We make this distinction because γ can be zero while the other parameters are all positive definite. To account for correlations among the gNFW parameters, we estimate their covariances from the best-fit parameters of the clusters in A10 and reproduce these covariances in our MC simulation. The cluster RXC J2319.6-7313 is removed from the A10 sample because its best-fit parameters are quite different from the rest of the sample. Additionally, we require that $\alpha > \gamma$ when generating the random parameters to avoid profiles that are uncharacteristic of the A10 sample. We note that c_{200} is treated as an independent variable, uncorrelated with the gNFW parameters.

We choose 200 M_{200} values logarithmically sampled from 30 to 3000 $\left[10^{13} M_\odot\right]$, and for each M_{200} 1000 realizations of SZE profiles are created. Since all AMiBA targets are massive clusters with at least $T_{\rm X} > 5$ keV, we include relativistic corrections assuming $T_{\rm X} = 10$ keV and note that changing $T_{\rm X}$ from 5 keV to 15 keV does not change the results significantly. Figure 18 shows the pair-wise scatter among the four free parameters for both the A10 clusters and our simulation. Figure 19 shows the gNFW profiles produced using both the A10 results and our simulation parameters.

Although we only show simulations here that model all the clusters together from A10, simulations that restrictively model either the cool-core or the disturbed subset of the cluster sample are done in an analogous way. Generally, we adjust our simulations to each cluster in order to connect its halo mass to its AMiBA flux.

The cosmology adopted in these simulations is a flat ΛCDM model with $H_0 = 67.1\,\mathrm{km\,s^{-1}\,Mpc^{-1}}$, $\Omega_{\rm m} = 0.3175$, and $T_{\rm CMB} = 2.725$ K (Planck Collaboration et al. 2014).

[14] $\beta = 5.4905$ is fixed in this simulation.

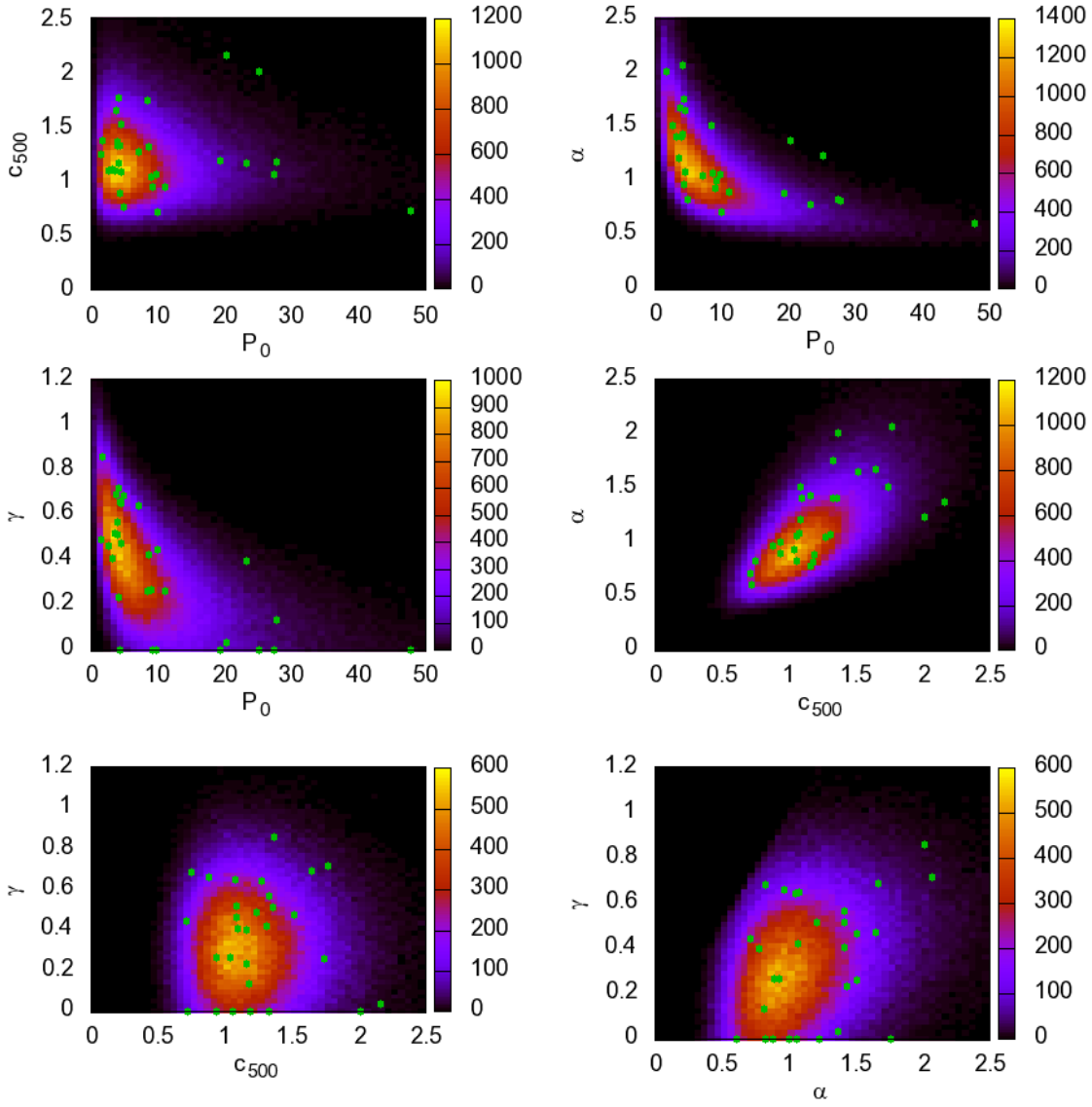

Figure 18. Pair-wise scatters among the gNFW parameters used in our Monte–Carlo simulations. Green points represent the best-fit parameters of the REXCESS clusters from A10. The color map shows the distribution of parameters used in this simulation. The color box indicates the counts in the linearly spaced histogram.

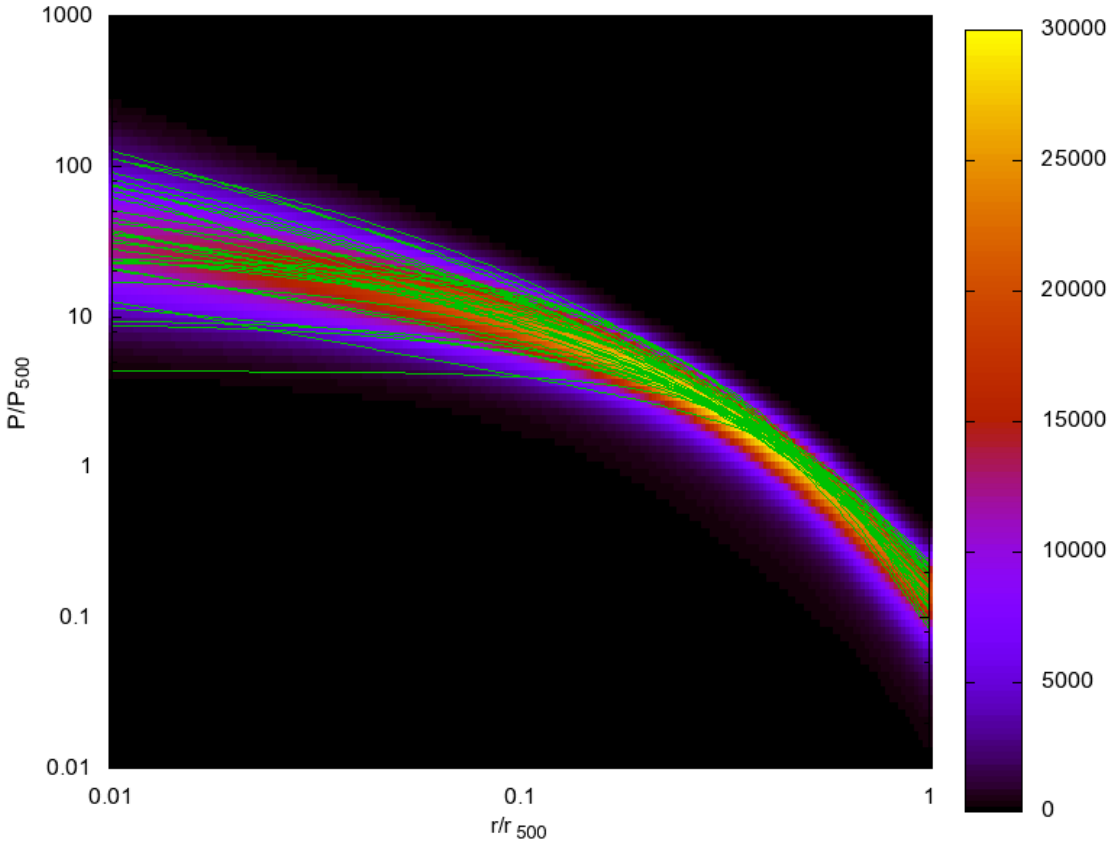

Figure 19. The gNFW profiles produced using parameters from Figure 18. The green lines correspond to the parameters from A10. Color scale indicates the number of the simulated profiles passing through each logarithmically-spaced grid cell.